

Dislocation density informed eigenstrain based reduced order homogenization modeling: verification and application on a titanium alloy structure subjected to cyclic loading

Yang Liu^{1,2,*}, Xiang Zhang^{2,†}, Yiguo Zhu¹, Ping Hu¹ and Caglar Oskay^{2,‡}

¹State Key Laboratory of Structural Analysis for Industrial Equipment
Faculty of Vehicle Engineering and Mechanics &
International Research Center for Computational Mechanics
Dalian University of Technology
Dalian, 116024, Peoples' Republic of China

²Department of Civil and Environmental Engineering
Vanderbilt University, Nashville, TN 37235, USA

Abstract

This manuscript presents a dislocation density informed eigenstrain based reduced order homogenization model (DD-EHM), and its application on a titanium alloy structure subjected to cyclic loading. The eigenstrain based reduced order homogenization (EHM) approach has been extended to account for the presence of HCP (primary α phase) and BCC (β phase) grains, within which the deformation process is modeled using a dislocation density based crystal plasticity formulation. DD-EHM has been thoroughly verified to assess the accuracy of the reduced order model in capturing local and global behavior compared with direct crystal plasticity finite element method (CPFEM) simulations. A structural scale study of titanium alloy Ti-6242S is performed using DD-EHM to quantify and characterize the spatial distribution and evolution of the dislocation pile-ups subjected to cyclic loading. The evolution of pileups at two spatial scales are tracked using a nonlocal parameter based on dislocation density discrepancy across neighboring grains. The effect of non-uniform texture on the response of the structural component has been investigated.

Keywords: Crystal plasticity, Titanium alloys, Dislocation Pile-ups, Multiscale modeling, Reduced order modeling

*Current affiliation: Department of Materials, Imperial College London, Exhibition Road, London, SW72AZ, UK.

†Current affiliation: Department of Mechanical Engineering, University of Wyoming, Laramie, WY, 82071, USA.

‡Corresponding author address: VU Station B#351831, 2301 Vanderbilt Place, Nashville, TN 37235. Email: caglar.oskay@vanderbilt.edu

1 Introduction

Predicting the response of structural components made of polycrystalline metals using microscopically informed multi-scale models requires efficient and accurate upscaling (homogenization) and downscaling (localization) strategies. In particular, the crystallographic physics that are local at the grain or subgrain scale must be retained during upscaling, and the computational cost must be sufficiently low to allow simulation of large structural components. Concurrent multiscale approaches such as the computational homogenization [1, 2], variational multiscale enrichment [3, 4, 5], heterogeneous multiscale method [6, 7], multiscale finite element method [8], among others provide the appropriate ways for rigorous scale bridging. Unfortunately, the high computational cost of these approaches limit their application to relatively small size problems.

While the high computational cost associated with these approaches can be alleviated by massive parallelization [9], employing reduced order approximations of the microstructure scale response is a more practical alternative and has been pursued by different researchers. A number of reduced order modeling approaches have been proposed and employed to efficiently replace crystal plasticity finite element method (CPFEM) simulations, including the classical Sachs and Taylor models, and more recent and sophisticated approaches such as spectral crystal plasticity method [10], grain cluster method [11], elasto-plastic self-consistent (EPSC) method [12, 13, 14], fast Fourier transform (FFT) method [15] and nonuniform transformation field analysis [16, 17]. Among others, sequential multiscale has been proposed as an alternative approach to devise structural scale models. In this approach, structural analysis is uncoupled from the microstructure scale, but a macro-scale constitutive model is trained based on microscale simulations on representative volume elements (RVEs) or statistical volume elements (SVEs), retaining local information in the form of internal state variables (e.g., [18, 19, 20]).

Recently, the eigenstrain based reduced order homogenization method (EHM) has been proposed to alleviate the computational cost of CPFEM simulations [21]. The EHM approach relies on the pre-computation of a small set of “constitutive tensors” that retain the microstructure morphological information, and employing these tensors to approximate the microstructure scale response fields using a much smaller basis obtained through constrained kinematics. EHM approach was later extended to achieve sparse and scalable formulations that allow efficient analysis of structures in the presence of large representative volumes by selectively eliminating long range interactions at the scale of the RVE [22]. An important advantage of the EHM is that the grain interactions and the intra-granular strain and stress variations with the microstructure could be retained during the up-scaling such that the individual grain information will be kept in the multiscale modeling.

In the aforementioned works, capabilities of the EHM approach was demonstrated in the context of the monotonic response of FCC polycrystals. In this manuscript, we extend the capabilities of the EHM framework to incorporate HCP, BCC and multi-phase microstructures subjected to monotonic and cyclic loading conditions. A reversible dislocation density based

56 crystal plasticity constitutive model is adopted to capture the dislocation evolution physics
57 under cyclic loading. The generalized crystal plasticity EHM implementation has been thor-
58 oughly verified to assess the accuracy of the reduced order model in capturing local and global
59 behavior compared with the direct CPFEM simulations. Structural scale investigations are
60 performed to study the spatial distribution of dislocation pile-ups in a large structure made of
61 titanium alloy, Ti-6Al-2Sn-4Zr-2Mo-0.1Si (Ti-6242S).

62 The remainder of the manuscript is organized as follows: In Section 2, the basic formulation
63 of the EHM approach and the dislocation density based crystal plasticity model are provided.
64 In Section 3, the dislocation density informed EHM framework is verified for HCP and BCC
65 crystals in direct comparison with CPFEM simulations. Section 4 provides the calibration
66 of model parameters using the experimental data for Ti-6242S; hereinafter, a component-level
67 analysis is conducted for this material to investigate dislocation pile-ups at the grain boundary
68 and the effect of non-uniform texture.

69 2 Eigenstrain based reduced order homogenization 70 for polycrystalline plasticity

71 The detailed derivation of the EHM approach in the context of computational homogenization
72 is provided in [21, 22]. A similar approach has been developed for variational multiscale
73 enrichment in [23, 24]. In what follows, we summarize the governing equations of the EHM
74 modeling approach and describe the dislocation density based evolution equations used to
75 describe the slip and hardening evolution within the material microstructure.

76 We consider the domain of a macroscopic structure, denoted as Ω . The structure con-
77 sists of a periodic construction of a polycrystalline microstructure, denoted as Θ . In what
78 follows, we loosely refer to the polycrystalline microstructure as the RVE indicating that the
79 microstructure is statistically representative in the context of ergodic measure of deforma-
80 tion. In order to ensure the applicability of the EHM approach, we make the following two
81 assumptions on the inelastic behavior within the structure: (1) the size of the macroscopic
82 spatial deformation wave form is large compared to the microstructure domain, i.e., the ma-
83 terial response is devoid of weak or strong discontinuities such as shear bands or cracks, and
84 that the classical scale separation assumption is valid; and (2) the strains at the scale of the
85 material microstructure remains small under the applied load cycles, and the material is taken
86 to undergo negligible amount of texture evolution. While texture evolution is an important
87 issue in a number of applications that involve large deformations, total micro- and macroscale
88 strains in fatigue problems often remain small (see, e.g., [25, 26] for near α titanium alloys)
89 and negligible texture evolution is observed.

90 In the context of the EHM approach, we consider the decomposition of the RVE into n
91 subdomains (or reduced order “parts”) such that $\Theta^{(\alpha)} \cap \Theta^{(\beta)} = \emptyset$ when $\alpha \neq \beta$; $\alpha, \beta = 1, 2, \dots, n$,
92 and $\cup_{\alpha=1}^n \Theta^{(\alpha)} = \Theta$, where $\Theta^{(\alpha)}$ denotes the domain of part α . The kinetics and the kinematics

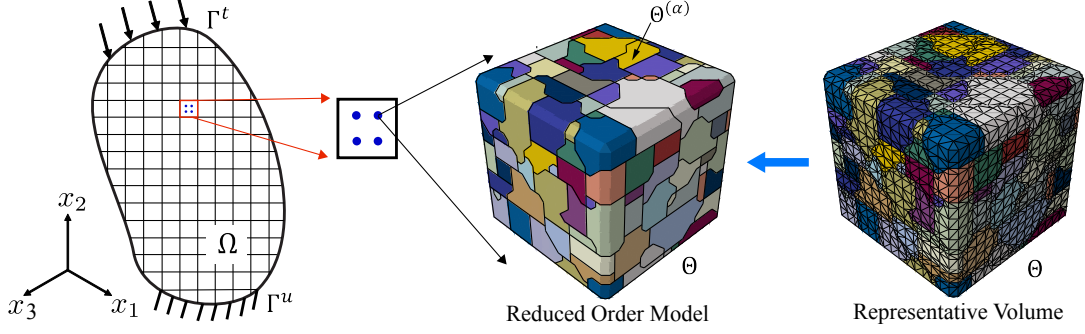


Figure 1: The two-scale problem: macro- and microscales.

93 in the reduced order model are constrained such that the stress and the visco-plastic strain
 94 fields are taken to spatially vary within the RVE in a piecewise constant fashion, based on the
 95 reduced order partitioning of the domain.

96 The boundary value problem governing the equilibrium at the macroscopic scale is ex-
 97 pressed as:

$$\nabla \cdot \bar{\boldsymbol{\sigma}}(\mathbf{x}, t) + \bar{\mathbf{b}}(\mathbf{x}, t) = 0 \quad \mathbf{x} \in \Omega; \quad t \in [0, t_0] \quad (1)$$

98 where, $\bar{\boldsymbol{\sigma}}$ is the macroscopic Cauchy stress; $\bar{\mathbf{b}}$ is the body force; and $\nabla \cdot$ denotes the divergence
 99 operator. The boundary conditions are given as:

$$\bar{\mathbf{u}}(\mathbf{x}, t) = \bar{\mathbf{u}}_0(\mathbf{x}, t) \quad \mathbf{x} \in \Gamma^u \quad (2)$$

$$\mathbf{n} \cdot \bar{\boldsymbol{\sigma}}(\mathbf{x}, t) = \bar{\mathbf{t}}_0(\mathbf{x}, t) \quad \mathbf{x} \in \Gamma^t \quad (3)$$

101 in which, $\bar{\mathbf{u}}$ denotes the macroscopic displacement field, $\bar{\mathbf{u}}_0$ and $\bar{\mathbf{t}}_0$ are the prescribed displace-
 102 ment and traction on the boundaries Γ^u and Γ^t , where $\Gamma^u \cup \Gamma^t = \partial\Omega$ and $\Gamma^u \cap \Gamma^t = \emptyset$. \mathbf{n} is the
 103 unit normal to Γ^t . The macroscale strain tensor, $\bar{\boldsymbol{\epsilon}}(\mathbf{x}, t)$ is expressed in terms of macroscale dis-
 104 placement based on small deformation assumption: $\bar{\boldsymbol{\epsilon}} = \nabla^s \bar{\mathbf{u}}(\mathbf{x}, t)$, where ∇^s is the symmetric
 105 gradient operator.

106 Considering the kinetic and kinematic approximations of the model reduction strategy and
 107 employing influence functions (i.e., discrete Green's functions) at the scale of the RVE to
 108 express the microscopic response fields, the part average stress and inelastic strain tensors for
 109 each part, β are related to each other as:

$$\mathbf{M}^{(\alpha\beta)} \dot{\boldsymbol{\sigma}}^{(\beta)}(\mathbf{x}, t) - \sum_{\alpha=1}^n [\mathbf{P}^{(\beta\alpha)} - \delta^{(\alpha\beta)} \mathbf{I}] \dot{\boldsymbol{\mu}}^{(\alpha)}(\mathbf{x}, t) = \mathbf{A}^{(\beta)} \dot{\boldsymbol{\epsilon}}(\mathbf{x}, t); \quad \beta = 1, \dots, n \quad (4)$$

110 where, $\boldsymbol{\sigma}^{(\alpha)}$ and $\boldsymbol{\mu}^{(\alpha)}$ respectively denote the part-averaged Cauchy stress and inelastic strain
 111 tensor associated with part α ; a superscribed dot over f indicates time derivative of f ; $\delta^{(\alpha\beta)}$
 112 is Kronecker delta ($\delta^{(\alpha\beta)} = 1$ if $\alpha = \beta$; $\delta^{(\alpha\beta)} = 0$ if $\alpha \neq \beta$); and \mathbf{I} is the fourth order identity
 113 tensor. $\mathbf{M}^{(\alpha\beta)}$, $\mathbf{P}^{(\beta\alpha)}$ and $\mathbf{A}^{(\beta)}$ are respectively the part-averaged compliance, interaction and
 114 concentration tensors. These tensors are integral functions of the influence functions providing

115 the morphological information of the RVE. The specific expressions for the coefficient tensors
 116 are provided in [21]. The macroscale stress is then computed as the volume average of the
 117 part-averaged stress coefficients:

$$\bar{\boldsymbol{\sigma}} = \sum_{\beta=1}^n \frac{|\Theta^{(\beta)}|}{|\Theta|} \boldsymbol{\sigma}^{(\beta)} \quad (5)$$

118 in which, $|\Theta^{(\beta)}|$ denotes the volume of part β and $|\Theta|$ is the volume of the RVE.

119 Since the static texture and dislocation slip are the sole sources of plastic deformation,
 120 inelastic strain in part α , $\boldsymbol{\mu}^{(\alpha)}$, results from dislocation slip over all slip systems within the
 121 grain that occupy $\Theta^{(\alpha)}$ through the Schmid law:

$$\dot{\boldsymbol{\mu}}^{(\alpha)}(\mathbf{x}, t) = \sum_{s=1}^N \dot{\gamma}^{s(\alpha)}(\mathbf{x}, t) \mathbf{Z}^{s(\alpha)} \quad (6)$$

122 in which, the superscript s denotes the s^{th} slip system in each part. $\mathbf{Z}^{s(\alpha)}$ is the Schmid
 123 tensor in part α , uniquely describing the orientation of the s^{th} slip system as the dyadic
 124 product of the slip direction, $\mathbf{n}^{s(\alpha)}$ and the direction normal to the slip plane $\mathbf{m}^{s(\alpha)}$ (i.e.,
 125 $\mathbf{Z}^{s(\alpha)} = \mathbf{n}^{s(\alpha)} \otimes \mathbf{m}^{s(\alpha)}$). N is the number of slip systems. The accuracy of the slip evolution
 126 naturally limits the reduced order discretization of the RVE. In particular, the RVE domain
 127 is discretized such that each part coincides with the domain or a subdomain of a single grain.
 128 By this approach, no averaging over slip systems within multiple grains forming a single part
 129 is necessary in the description of slip and hardening evolution. This constraint implies that
 130 the coarsest reduced order discretization corresponds to the case when each part occupies
 131 the domain of a single grain, in what follows referred to as the *one-part-per-grain* model.
 132 Under this constraint, the compliance tensor of each part is equal to the compliance tensor
 133 of corresponding grain within the RVE. If a grain is divided into multiple separate parts, the
 134 resulting reduced model is referred to as a *multi-part-per-grain* model. The consequences of
 135 grain partitioning is investigated in Section 3.2.

136 The above mentioned reduced-order formulation relies on the assumption of piece-wise con-
 137 stant spatial distribution of the inelastic strain field within the RVE. It is possible to choose
 138 other, more complex forms of spatial distribution functions to represent the inelastic strain
 139 field, such as non-uniform plastic modes [27, 17]. When the approximate direction of the ap-
 140 plied loading (i.e., the history of macroscopic strain field) on the microstructure is known a
 141 priori, very accurate plastic modes could be identified through proper orthogonal decompo-
 142 sition and the resulting reduced order model could yield higher accuracy than the piece-wise
 143 constant approximation. A critical benefit of employing piece-wise constant approximation is
 144 that the construction of the reduced order model is purely geometrical and does not rely on
 145 prior knowledge of the direction of loading on the microstructure, which is typically unknown
 146 and time-varying in the context of a multiscale simulation. While it is possible to also con-
 147 sider adaptive enrichment of the approximation basis during a multiscale analysis to improve
 148 accuracy, this step is typically considerably expensive from the computational point of view.

2.1 Reversible dislocation density based crystal plasticity under cyclic loading

The classical dislocation-mediated plasticity was first introduced by [28, 29] and [30]. Based on these fundamental theories, major progress has been made in the development of dislocation density based crystal plasticity constitutive models in the past few decades (see e.g., [31, 32, 33]). These constitutive models have been shown to reveal the underlying plastic deformation mechanisms in various metallic material microstructures, validated by experimental observations [12, 34, 35]. Langer and co-authors have recently developed an alternative, physics-based plasticity theory consistent with the thermodynamics principles. This theory proposes an advanced dislocation model, which incorporates the energy and entropy in the dislocation flow in the presence of strain rate sensitivity and non-uniform Bauschinger effects [36, 37, 38]. In this manuscript, the classical dislocation theory has been adopted, but the modeling strategy can be extended to incorporate others in a straightforward manner.

In what follows, the part index α is omitted in the equations for simplicity, but the variables are to be understood as part-averaged quantities. The slip rate at the s^{th} slip system is derived from the Orowan's equation and expressed as [39, 35]:

$$\dot{\gamma}^s = \frac{\rho_m^s \nu_{id}^s (b^s)^2}{2} \text{sgn}(\tau^s) \exp\left(\frac{-\Delta F^s}{k\theta}\right) \exp\left(\frac{(\tau^s - s^s)\Delta V^s}{k\theta}\right) \quad (7)$$

where, s^s is the critical resolved shear strength (CRSS), ΔV^s is the thermal activation volume, k the Boltzmann constant ($1.38 \times 10^{-23} \text{ J} \cdot \text{K}^{-1}$) and θ the temperature in Kelvin. In Eqn. (7), $\dot{\gamma}^s$ is related with ρ_m^s , the average mobile dislocation density, ν_{id}^s , the vibration frequency of the dislocation segment, b^s , the magnitude of the Burgers vector and ΔF^s , the activation energy. The resolved shear stress τ^s is associated with the Cauchy stress through \mathbf{Z}^s as:

$$\tau^s = \boldsymbol{\sigma} : \mathbf{Z}^s \quad (8)$$

In addition, it has been widely acknowledged that the stored sessile dislocation would be the main source for fatigue deformation behaviour, such as local strain or stress concentration and strengthening [26, 40, 41], including geometrically necessary dislocation and stored statistical dislocation density. Thus, here the strength hardening evolution in HCP dominated crystals are expressed as [31, 42]:

$$s^s(\dot{\gamma}^s) = s_0^s + s_{\text{for}}^s(\dot{\gamma}^s) + s_{\text{deb}}^s(\dot{\gamma}^s), \quad (9)$$

in which, s_0^s is the temperature-dependent initial slip resistance. s_{for} and s_{deb} respectively denote the contributions to strength evolution by the sessile (i.e., forest and debris) dislocations, described as

$$s_{\text{for}}^s(\dot{\gamma}^s) = \mu\chi b^s \sqrt{\rho_{\text{for}}^s} \quad (10)$$

$$s_{\text{deb}}^s(\dot{\gamma}^s) = \mu b^s k_{\text{deb}} \sqrt{\rho_{\text{deb}}^s} \ln\left(\frac{1}{b^s \sqrt{\rho_{\text{deb}}^s}}\right), \quad (11)$$

179 where, μ is the shear modulus, χ the dislocation interaction parameter (set to 0.9) satisfying
 180 the Taylor relationship [31]. The latent hardening effects have not been incorporated in this
 181 study, because dislocation density evolution induced by latent hardening has been found to be
 182 small compared with that due to self-hardening in the alloys investigated here [43, 34, 44]. The
 183 latent hardening effects could be added by replacing the scalar χ with an interaction coefficient
 184 matrix as employed in [42]. $k_{\text{deb}} = 0.086$ is the material independent factor associated with
 185 low substructure dislocation density [32]. ρ_{for}^s and ρ_{deb}^s are the forest and debris dislocation
 186 densities, respectively.

187 Experimental observations by [45, 33, 46, 47] indicate that the forest and debris dislocations
 188 and their evolution significantly impact the mechanical behavior of HCP and BCC polycrys-
 189 talline materials. Under monotonic loading, the forest dislocation density evolves through the
 190 competing mechanisms of generation and annihilation associated with recovery [12]. The evo-
 191 lution is affected by the current dislocation density as well as the extent of plastic slip. Stored
 192 forest dislocations annihilate by the effect of shearing along the opposing strain path when the
 193 loading is reversed under cyclic loading conditions [48, 14]. The total forest dislocation density
 194 is expressed as:

$$\rho_{\text{for}}^s = \rho_{\text{fwd}}^s + \rho_{\text{rev}}^{s+} + \rho_{\text{rev}}^{s-} \quad (12)$$

195 where, ρ_{fwd}^s is the forward dislocation density and $\rho_{\text{rev}}^{s\pm}$ denote the reversible terms correspond-
 196 ing to loading and unloading paths along the s th slip system as shown in Fig. 2. Superscripts
 197 $s+$ and $s-$ denote the particular slip direction in the slip system. The initial forest disloca-
 198 tion density is relatively low in the pure HCP- or BCC-based materials corresponding to the
 199 experimental observations [49, 33, 45, 50] and a small value $\rho_{\text{for},0} = 1.0 \times 10^{12} \text{ m}^{-2}$ is used for
 200 materials considered in this study. The evolution of the forward term is expressed as:

$$\frac{\partial \rho_{\text{fwd}}^s}{\partial \gamma^s} = (1 - p) \frac{\partial \rho_{\text{gen,fwd}}^s}{\partial \gamma^s} - \frac{\partial \rho_{\text{rec,fwd}}^s}{\partial \gamma^s} = (1 - p) k_1^s \sqrt{\rho_{\text{for}}^s} - k_2^s(\dot{\gamma}, \theta) \rho_{\text{for}}^s, \quad (13)$$

201 where $\rho_{\text{gen,fwd}}^s$ and $\rho_{\text{rec,fwd}}^s$ are the athermal storage and temperature dependent recovery of
 202 classical Kock-Mecking law [51]. p is a reversibility parameter determining the fraction of the
 203 reversible loosely tangled forest dislocations. Since the shear strain is relatively small in cyclic
 204 loading, a greater value of $p = 0.8$ is chosen according to [48]. k_1^s and k_2^s are the coefficients
 205 controlling the generation of forest dislocations and the annihilation due to dynamic recovery,
 206 respectively. The recovery coefficient is taken to be proportional to generation rate:

$$k_2^s(\dot{\gamma}^s, \theta) = k_1^s \frac{b^s \chi}{g^s} \left[1 - \frac{k\theta}{\widehat{D}^s b^{s3}} \ln \left(\frac{\dot{\gamma}^s}{\dot{\gamma}_0} \right) \right] \quad (14)$$

207 Equation 14 is similar to the law proposed in [31], but employs the slip rate of the current slip
 208 system rather than the total strain rate. $\dot{\gamma}_0$, g^s and \widehat{D}^s are respectively the reference shearing
 209 rate defined as 10^7 s^{-1} (satisfying the high cycle and low cycle fatigue loading conditions),
 210 effective activation enthalpy and drag stress. The evolutions of the remaining components of

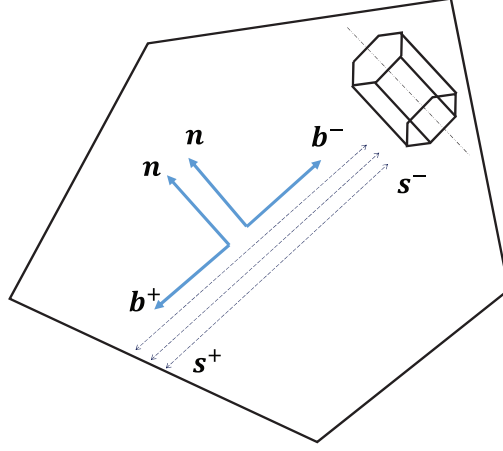


Figure 2: Slip orientations for the reversible dislocation density evolution.

211 the forest dislocation density are expressed as functions of the loading direction along the slip
 212 system [48]:

Case 1 : if $\tau^s > 0$

$$\begin{aligned} \frac{\partial \rho_{\text{rev}}^{s+}}{\partial \gamma^s} &= pk_1^s \sqrt{\rho_{\text{for}}^s} - k_2^s(\dot{\gamma}^s, \theta) \rho_{\text{rev}}^{s+} \\ \frac{\partial \rho_{\text{rev}}^{s-}}{\partial \gamma^s} &= -k_1^s \sqrt{\rho_{\text{for}}^s} \left(\frac{\rho_{\text{rev}}^{s-}}{\rho_0^s} \right)^{\hat{m}} \end{aligned} \quad (15)$$

213

Case 2 : if $\tau^s < 0$

$$\begin{aligned} \frac{\partial \rho_{\text{rev}}^{s-}}{\partial \gamma^s} &= pk_1^s \sqrt{\rho_{\text{for}}^s} - k_2^s(\dot{\gamma}^s, \theta) \rho_{\text{rev}}^{s-} \\ \frac{\partial \rho_{\text{rev}}^{s+}}{\partial \gamma^s} &= -k_1^s \sqrt{\rho_{\text{for}}^s} \left(\frac{\rho_{\text{rev}}^{s+}}{\rho_0^s} \right)^{\hat{m}} \end{aligned} \quad (16)$$

214 where, ρ_0^s is the value of the total dislocation density at the point of load reversal and \hat{m} is the
 215 dislocation density recombination coefficient taken to be 0.4 for HCP and BCC crystals [14].
 216 The state of $\tau^s = 0$ incurs no plastic flow or dislocation density evolution. It is worthy to
 217 note that τ^s is the part-averaged Cauchy stress σ resolved onto the s^{th} slip system. Thus, the
 218 change in sign of τ^s does not necessarily correspond to the load reversals in the macroscopic
 219 load cycles.

220 The recovery process through dislocation climb or cross-slip is naturally related to the
 221 debris dislocation formation. Thus, the evolution rate of debris dislocation density is taken to
 222 be proportional to the recovery rate. As implied by Eq. 11, hardening at a given slip system,
 223 s , is taken to be affected by the total debris dislocations on all slip systems. The evolution of

224 the debris dislocation density is expressed as the sum of contributions from each slip system:

$$d\rho_{\text{deb}} = \sum_s \frac{\partial \rho_{\text{deb}}^s}{\partial \gamma^s} d\gamma^s \quad (17)$$

225 where,

$$\begin{aligned} \frac{\partial \rho_{\text{deb}}^s}{\partial \gamma^s} &= qb^s \sqrt{\rho_{\text{deb}}} \frac{\partial \rho_{\text{rec,fwd}}^s}{\partial \gamma^s} \rho_{\text{for}}^s \\ &= qb^s \sqrt{\rho_{\text{deb}}} k_2^s(\dot{\gamma}^s, \theta) \rho_{\text{for}}^s \end{aligned} \quad (18)$$

226 where, q is the recovery rate coefficient. The initial debris dislocation density in all slip systems
 227 is defined as the same quantity, $\rho_{\text{deb},0}^s = 1.0 \times 10^{10} \text{ m}^{-2}$ [52, 53].

228 The dislocation density based crystal plasticity model defined in Eqs. 7-18 has been imple-
 229 mented within the EHM framework (Eqs. 1-6). In contrast to the classical crystal plasticity
 230 finite element approach, the evolution equations and the state variables are associated with
 231 each reduced model part rather than a material point. The implementation has been performed
 232 by employing the commercial finite element package, ABAQUS. The reduced order model is
 233 incorporated using the user supplied material subroutine capabilities. A two-level semi-implicit
 234 stress integration algorithm is applied to obtain the convergence of Cauchy stress and CRSS.
 235 In the first level, Newton-Raphson algorithm is used to calculate the stress update with full-
 236 implicit integration. Then the dislocation densities and CRSS are explicitly updated. The two
 237 steps of the integration process is repeated until convergence.

238 3 DD-EHM model verification

239 The accuracy characteristics of the reduced order model (referred to as DD-EHM in what
 240 follows) introduced in the previous section are verified against classical CPFEM simulations at
 241 the microstructure scale [54, 55, 56]. The model is not restricted to specific evolution laws. We
 242 therefore employ a bottom-up verification approach where, the proposed model is verified using
 243 a pure HCP (Magnesium) and a pure BCC (Niobium) microstructures first. The capability of
 244 the model is then demonstrated in a more complex alloy (Section 4). In the current section,
 245 the effect of the model order in capturing the local stress distribution within the RVE is also
 246 investigated. In the next section, the verified model has been further demonstrated using a
 247 more complex two-phase alloy. Verification of the EHM approach for multi-phase materials (in
 248 FCC polycrystals) has been performed in [5]. Twinning, an important deformation mechanism,
 249 could also be incorporated in the EHM formulation. For simplicity of the verification studies,
 250 twinning is not included in the description of plastic deformation.

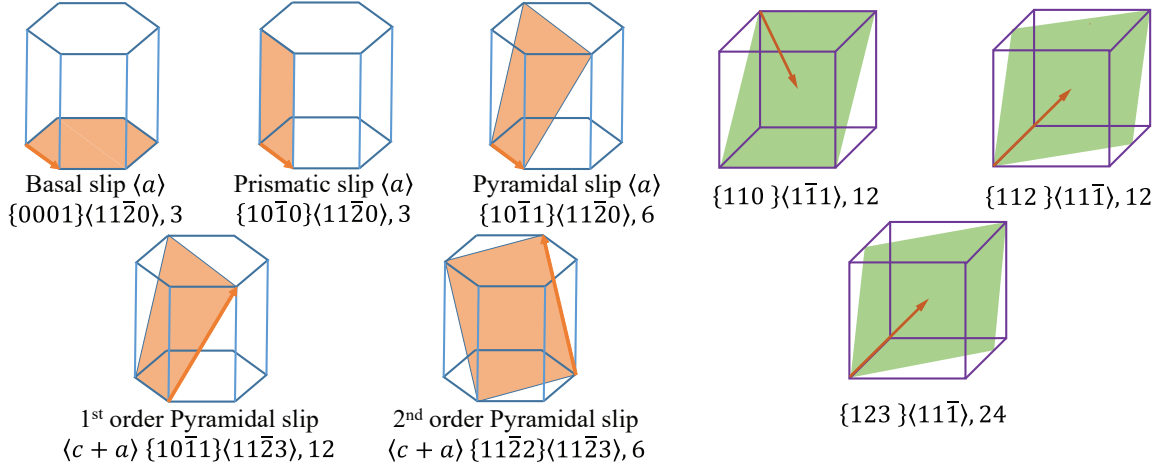


Figure 3: Slip systems in HCP and BCC lattices.

3.1 Single phase HCP or BCC polycrystal verification

The model verifications have been performed for material behavior that does not exhibit severe strain softening (e.g. shear bands) where deformation localizes at a length scale below the size of the RVE [57]. The verifications are performed by comparing the results of the proposed DD-EHM approach with those of the CPFEM simulations (i.e., the reference model) performed on a representative volume. Figure 4 illustrates a sample microstructure employed in the verification analyses. The grain orientations are sampled from the uniform orientation distribution function which contains 145 grains and is generated by the previous workflow [21, 35]. The DD-EHM model employs a part-per-grain model reduction approach (i.e., $n = 145$). Identical constitutive models (Section 2.1) and constitutive parameters (Table 1) have been employed in the DD-EHM and CPFEM simulations. The full field CPFEM simulation contains 82,561 four-noded tetrahedra elements.

Table 1 summarizes the model parameters of the HCP and BCC grains, respectively, used in the model verification studies. The slip systems considered for the HCP and BCC lattices are shown in Fig. 3. The HCP model includes 30 slip systems including the basal, pyramidal and prismatic systems. The parameters are obtained based on the stress-strain behavior of magnesium polycrystals provided by [58]. The BCC model includes 48 slip systems, and the model parameters are obtained based on the curves provided in [34] for niobium polycrystals. The mobile dislocation density within a grain is likely to be different for different slip systems and evolves with deformation, however it remains difficult to experimentally quantifying the magnitude and evolution of mobile dislocations. In this study, its value is taken to be constant and set to the same in all slip systems following Ref. [40].

Figure 5 shows the comparison of the RVE-averaged (i.e., overall) stress strain behavior for the proposed and the reference models for a pure HCP polycrystal subjected to strain controlled uniaxial tension, fatigue cycle, dwell fatigue cycle and a more complex biaxial load path. The overall stress reported for CPFEM simulations are calculated by volume-averaging

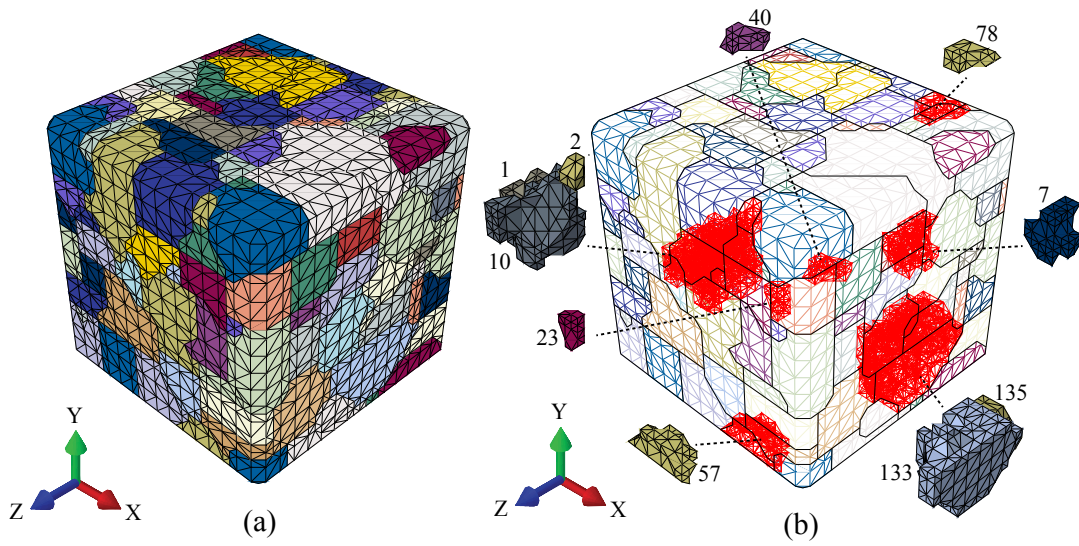


Figure 4: Sample microstructure used in verification. (a) Discretization used in the CPFEM simulations; (b) Selected grains used in the verification of the DD-EHM simulations.

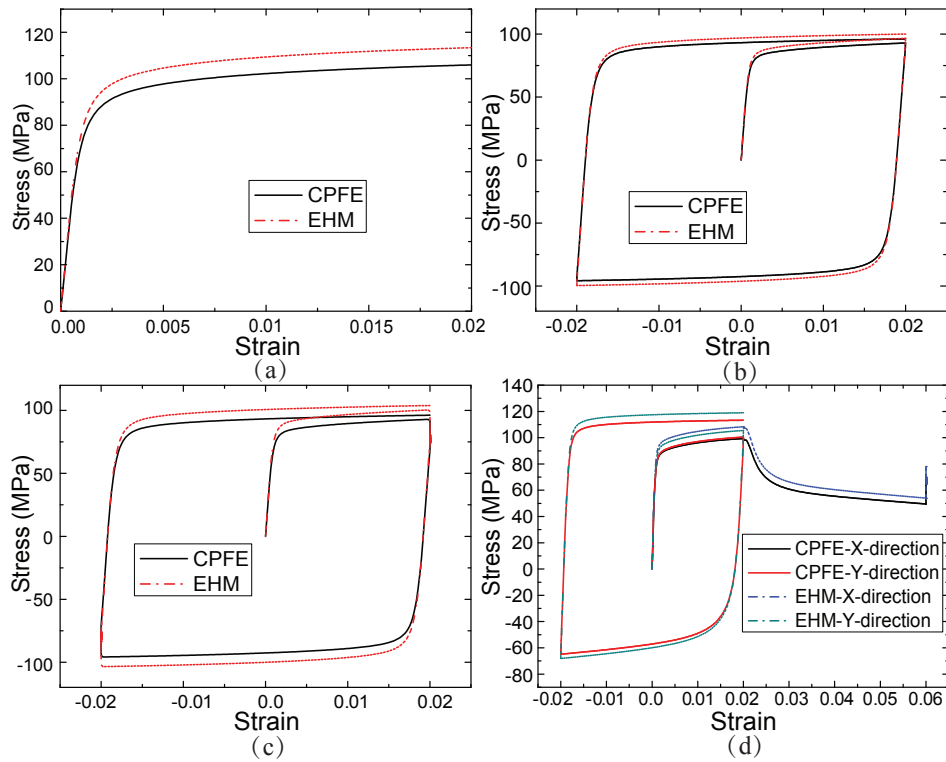


Figure 5: Overall stress-strain curves for the HCP polycrystal subjected to: (a) uniaxial tension; (b) pure fatigue cycle; (c) dwell fatigue cycle; (d) biaxial loading.

Table 1: Model parameters for the HCP and BCC crystals used in the verification studies.

Parameters		HCP				BCC
Symbols	Units	Basal $\langle a \rangle$	Prismatic $\langle a \rangle$	Pyramidal $\langle a \rangle$	Pyramidal $\langle c + a \rangle$	$\{110\}\{\bar{1}\bar{1}1\}$
ΔF^s	J	2.58×10^{-19}	2.93×10^{-19}	3.21×10^{-19}	3.44×10^{-19}	2.27×10^{-19}
ΔV^s	m^3	1.94×10^{-29}	2.84×10^{-29}	2.96×10^{-29}	3.17×10^{-29}	4.79×10^{-27}
ρ_m^s	m^{-2}	5.00×10^{12}	5.00×10^{12}	5.00×10^{12}	5.00×10^{12}	5.00×10^{12}
ν_{id}^s	Hz	1.00×10^{12}	1.00×10^{12}	1.00×10^{12}	1.00×10^{12}	1.00×10^{12}
b^s	μm	3.54×10^{-4}	3.58×10^{-4}	3.59×10^{-4}	6.83×10^{-4}	2.86×10^{-4}
s_0^s	MPa	11.60	47.20	143.69	158.87	94.00
k_1^s	m^{-1}	6.32×10^6	1.07×10^8	1.03×10^8	1.74×10^8	5.20×10^7
D^s	MPa	100	150	185	225	230

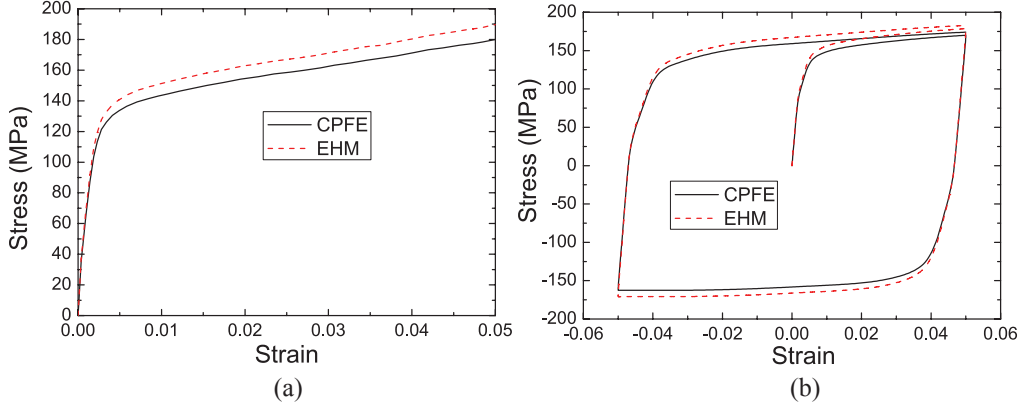


Figure 6: Overall stress-strain curves for the BCC polycrystal subjected to: (a) uniaxial tension; (b) pure fatigue cycle.

277 of element-wise stresses in the RVE. In the uniaxial tension case (Fig. 5a), a 2 % strain is
 278 applied along the X -direction with a constant strain rate of 0.05 s^{-1} . In the fatigue cycle
 279 case (Fig. 5b), a maximum strain amplitude of 2 % is applied along the X -direction at strain
 280 rate of 0.04 s^{-1} . The R -ratio is set to $R = -1$. In the dwell fatigue cycle case (Fig. 5c),
 281 the same maximum strain, strain rate and R -ratio are applied along the X -direction. Upon
 282 reaching maximum strain in tension and compression, the strain is held for 0.5s before the
 283 loading is reversed. In the biaxial loading case (Fig. 5d), a 6 % tensile strain is applied at the
 284 X -direction with constant strain rate of 0.04 s^{-1} and the strain is held until the end of the
 285 test. Concurrently, the RVE is subjected to a cyclic load with a peak strain of 4 % along the
 286 Y -direction at 0.04 s^{-1} strain rate and with $R = -1$. The total duration of the cyclic biaxial
 287 tension and the fatigue cycle tests are 2.5 s, whereas the total time of the dwell fatigue cycle
 288 testing is 3.5 s. In Figure 6, the comparison between the proposed and the CPFEM model
 289 is shown for the BCC polycrystal subjected to strain controlled uniaxial tension and fatigue
 290 cycle. The same loading rate, total strain and R -ratio are applied in the BCC case.

291 Figures 5 and 6 illustrate that the overall stress-strain behavior predicted by the proposed
 292 approach matches well with the reference CPFEM simulations. DD-EHM shows slightly stiffer

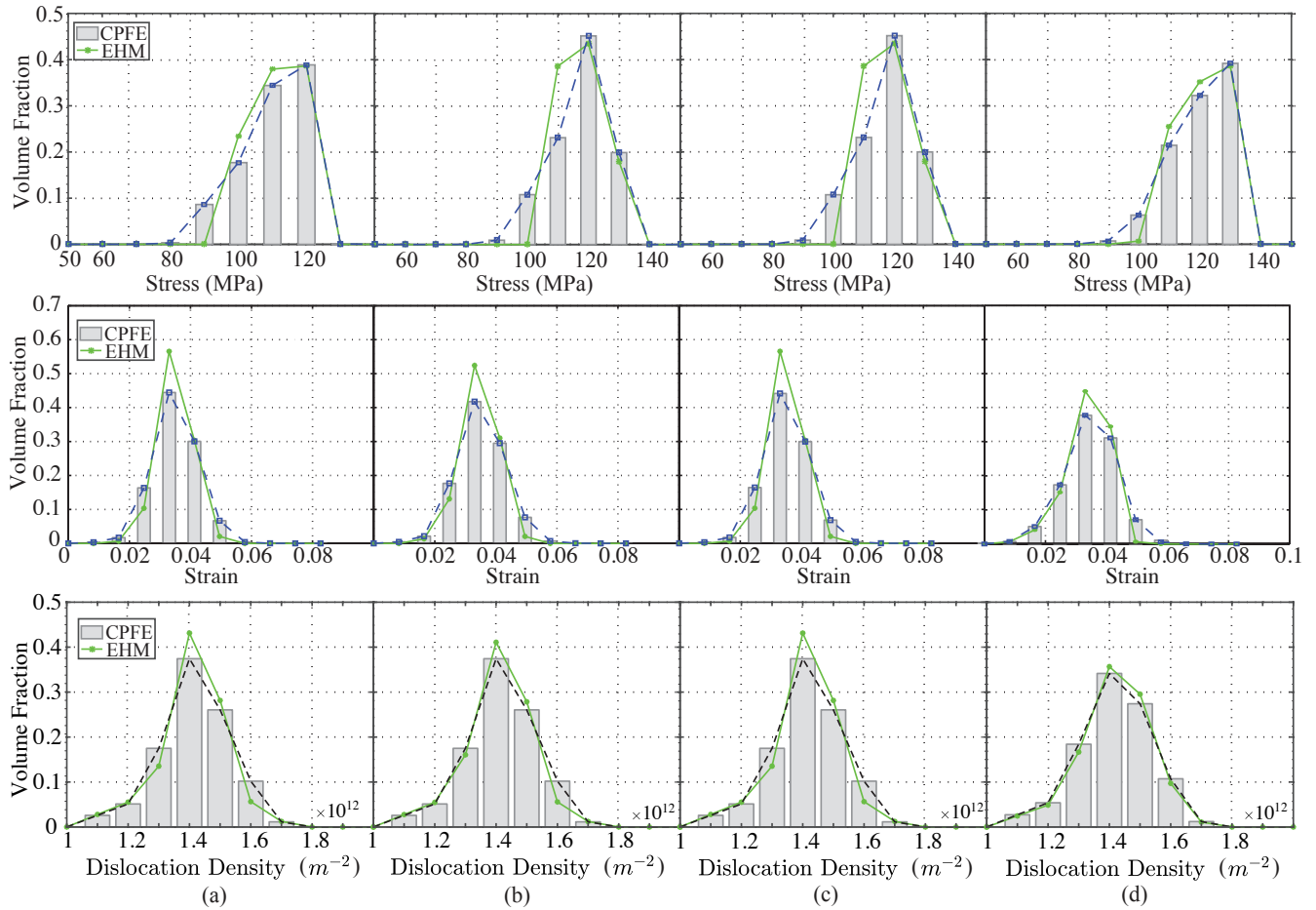


Figure 7: Local Mises stress, principal strain and dislocation density distributions at the peak load for the HCP polycrystal subjected to: (a) uniaxial tension; (b) pure fatigue cycle; (c) dwell fatigue cycle; and (d) biaxial loading.

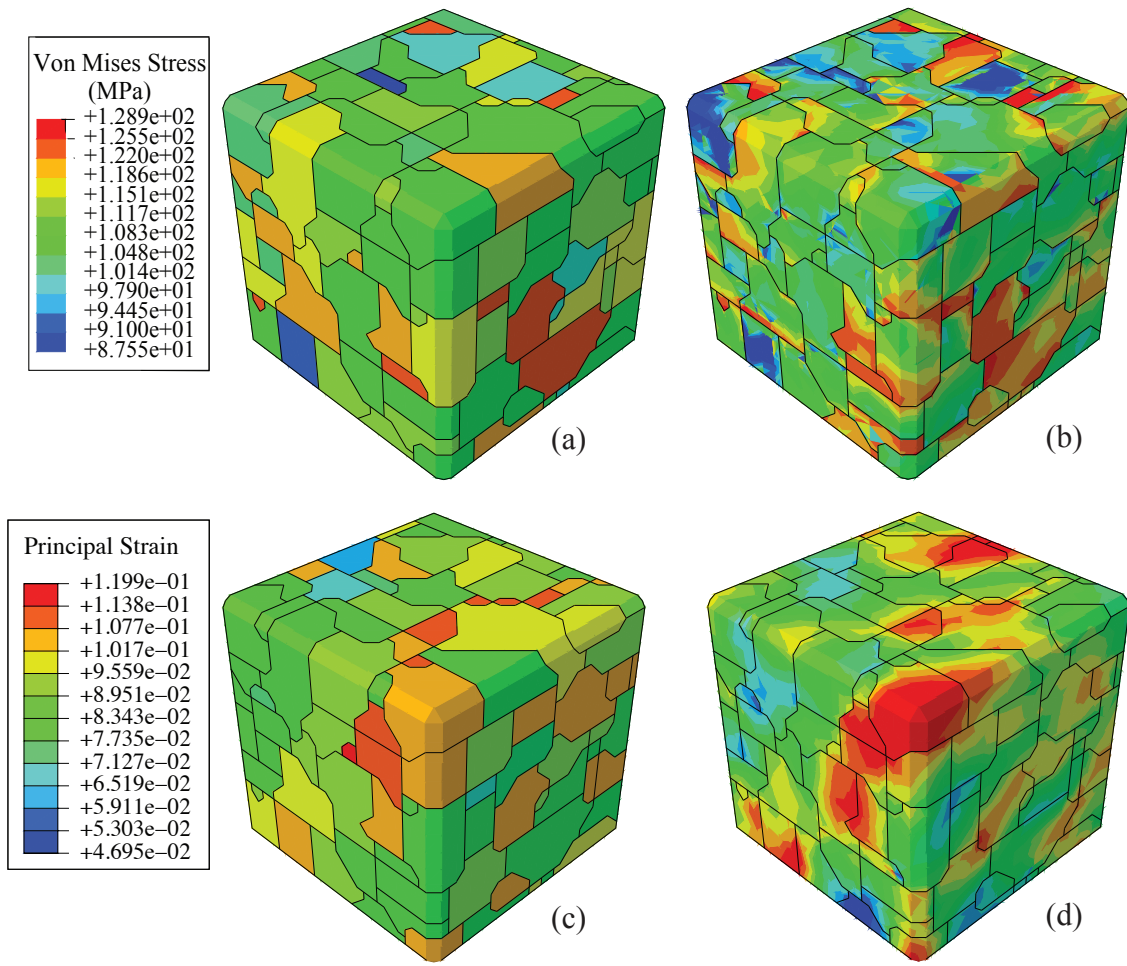


Figure 8: Local Mises stress contours for the HCP microstructure using: (a) DD-EHM model; (b) CPFEM model. Local maximum principal strain contours using: (c) DD-EHM model; (d) CPFEM model.

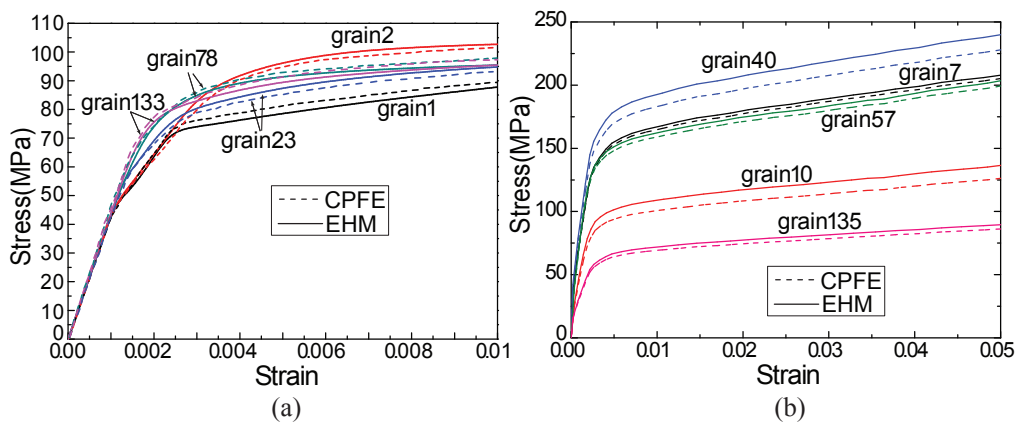


Figure 9: Stress-strain curves comparison of 5 random grains chosen in the (a) HCP and (b) BCC polycrystals under uniaxial tension.

293 responses compared with the reference case due to constrained kinematics associated with the
294 reduced basis. In order to ensure the consistency of the accuracy, 50 separate uniaxial tension
295 simulations were performed with random grain orientations sampled from uniform orientation
296 distribution. The error in the overall stress-strain curves as defined by the discrete L2 norm
297 were bounded by approximately 10 % for all cases considered. As a reference for accuracy
298 of model predictions, experiments on Ti-6242S exhibited about 5% variation in flow stress
299 predictions at low temperature and about 12% variation at high temperatures [59].

300 In addition to the overall stress responses, we tested the ability of the DD-EHM model in
301 capturing the local stress variations within the microstructure. Figure 7 shows the comparison
302 of the local stress, strain and dislocation density distributions between the proposed approach
303 and the CPFEM simulations at the peak load state of all four loading conditions applied to
304 the HCP polycrystal. Using the form of a histogram plot, the volume fraction of grains within
305 the microstructure are plotted as a function of the stress and strain levels experienced by
306 the grains. The bin plots represent the CPFEM model whereas the stars at the mid-point of
307 each bin refer to the proposed model. The magnitudes of the local stresses match well with
308 those of the reference simulations under the four loading conditions. The magnitudes of the
309 local strains deviate slightly more than the respective stress distributions under the four loading
310 conditions with peak strain amplitudes underestimated by the proposed approach. Dislocation
311 density distribution patterns are similar to that of strain distributions. Figure 8 illustrates
312 the variation of equivalent stress and maximum principal strain within the RVE as predicted
313 by the DD-EHM and CPFEM approaches. The contour plots are from the biaxial loading at
314 the end of the loading period. The CPFEM simulation captures the spatial variation of the
315 stresses and strains within each grain, whereas the part-per-grain DD-EHM model tracks a
316 grain-averaged fields only.

317 Figure 9 compares the stress-strain curves at a number of grains within the microstructure
318 shown in Figure 4. The results indicate that the accuracy of the DD-EHM in capturing the local
319 stresses are bounded by approximately 13.4 % error. Implemented with the dislocation density
320 based constitutive law, the EHM has the similar accuracy of the local grain-scale responses in
321 keeping with CPFEM results, compared with the previous EHM numerical results [21].

322 **3.2 Hierarchical model improvement: sub-grain responses pre-** 323 **diction**

324 In polycrystalline microstructures with high anisotropy or in the presence of multiple phases
325 with high property contrast, stress and deformations could vary significantly within each grain
326 and concentrate near the grain/phase boundaries and triple junctions. In the proposed reduced
327 order modeling approach, the variability of the response fields within each grain could be better
328 approximated by considering larger number of reduced order parts per each grain (denoted
329 as multi-part-per-grain approximation). The multi-part-per-grain approximation therefore
330 considers a non-uniform variation of the inelastic response field within each grain.

331
332
333
334
335
336
337
338
339
340
341

In this section, the effect of using a multi-part-per-grain scheme and improvement of accuracy with increasing model order are investigated. The investigations are performed on an idealized microstructural configuration that contains 13 grains as shown in Fig. 10a. The idealized microstructure is subjected to uniaxial tension along the X direction up to 5 % total strain with 0.05 s^{-1} strain rate. Five different reduced order models with hierarchically increasing orders are considered starting from part-per-grain (i.e., 13 parts as shown in Fig. 10a) up to 136 parts (Fig. 10e). The grains are taken to be HCP with random orientations sampled from uniform orientation distribution. The material parameters summarized in Table 1 are used. For each DD-EHM model as well as the reference CPFEM approach, 50 simulations are performed using randomly sampled orientations for each grain. The full field CPFEM discretization contains 62,513 four-noded tetrahedra elements.

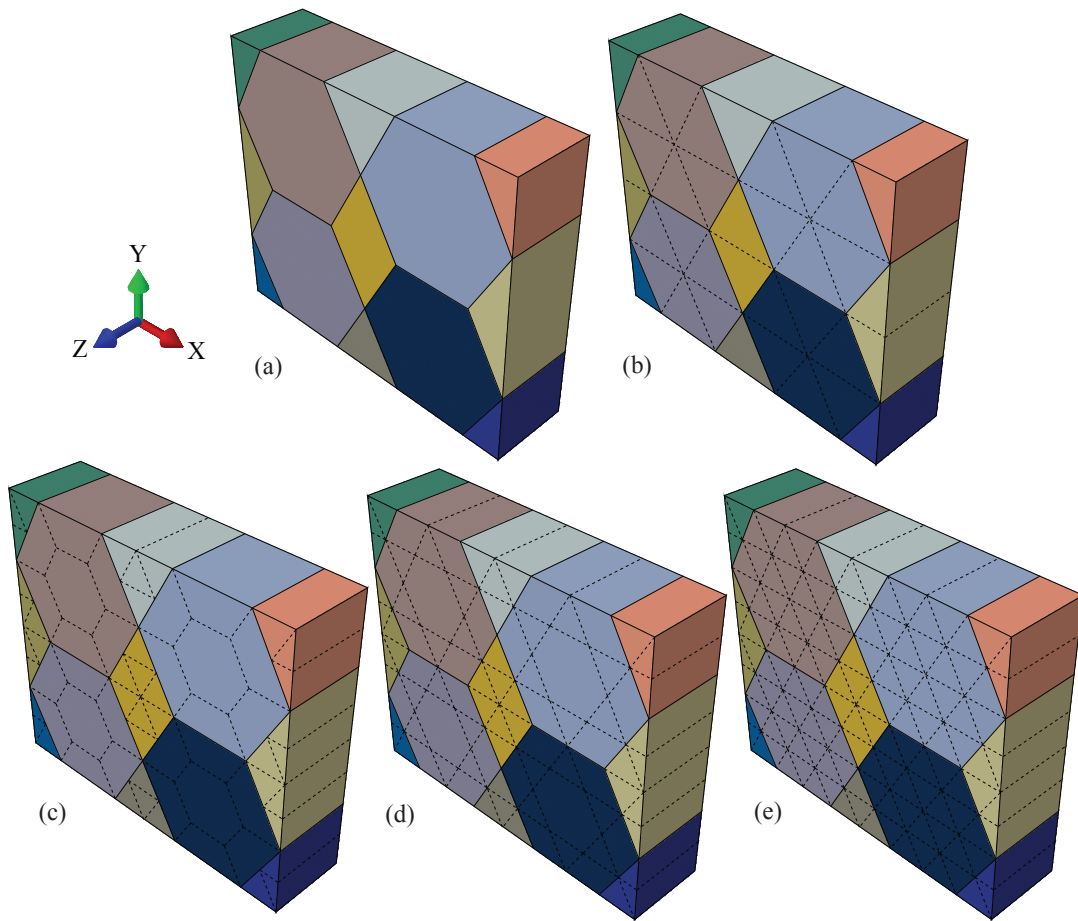


Figure 10: Partitioning schemes: (a) simple grain partition (13 parts); (b) triangular prism partition (36 parts); (c) surface grain contact partition (adjacent grain; 68 parts); (d) triple junction partition (92 parts); (e) refined triangular prism partition (136 parts).

342
343
344

In comparison with the CPFEM model, the overall stress-strain curves and local stress distributions are presented in Fig. 11. The figure is from one out of 50 sets of simulations. All 50 sets exhibit relatively similar error distributions with the plots showing close to average

345 errors. The figure shows that as the partition number increases, the overall response of the
 346 DD-EHM model improves by a small amount. In contrast, the distribution of local stresses
 347 (Fig. 11b) significantly improves as a function of model order. This result indicates that model
 348 refinement would lead to further improvement in capturing the local response fields within the
 microstructure.

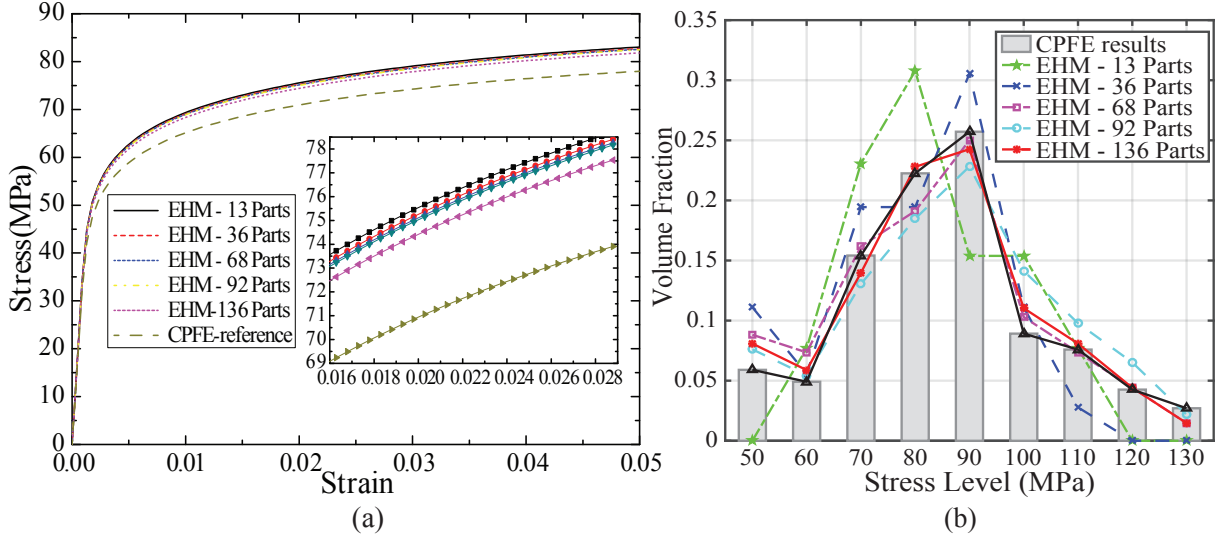


Figure 11: DD-EHM model refinement study: (a) Overall stress vs. strain curves; (b) Local stress distributions

349
 350 Figure 12 shows the stress distributions predicted by the reduced order models at the
 351 peak strain amplitude and compared to that of the reference simulation. The figure indicates
 352 that not only that the local stress distributions improve as a function of the increased model
 353 order, but that the stress concentrations within the microstructures are predicted in reasonable
 354 accuracy. The high stress regions that occur near the triple points and grain boundaries are
 355 captured in a progressively more accurate manner as a function of the model hierarchy.

356 The assessment of model error as a function of model order across all 50 sets of simulations
 357 are shown in Fig. 13. The error is defined as:

$$\text{error} = \int_0^\epsilon \frac{|\sigma_{\text{DD-EHM}} - \sigma_{\text{CPFEM}}|}{\sigma_{\text{CPFEM}}} d\epsilon \quad (19)$$

358 Figure 13a indicates that the error magnitude is stable and approximately range between 2 %
 359 and 10 % across 50 simulations regardless of the model order. While the mean error does not
 360 appear to be significantly reduced, confirming the above mentioned results, the variance in the
 361 predictions are smaller with higher model order as shown in Fig. 13b.

362 The speedup Q of the DD-EHM model compared with CPFEM calculation,

$$Q = \frac{t_{\text{CPFEM}}}{t_{\text{DD-EHM}}} \quad (20)$$

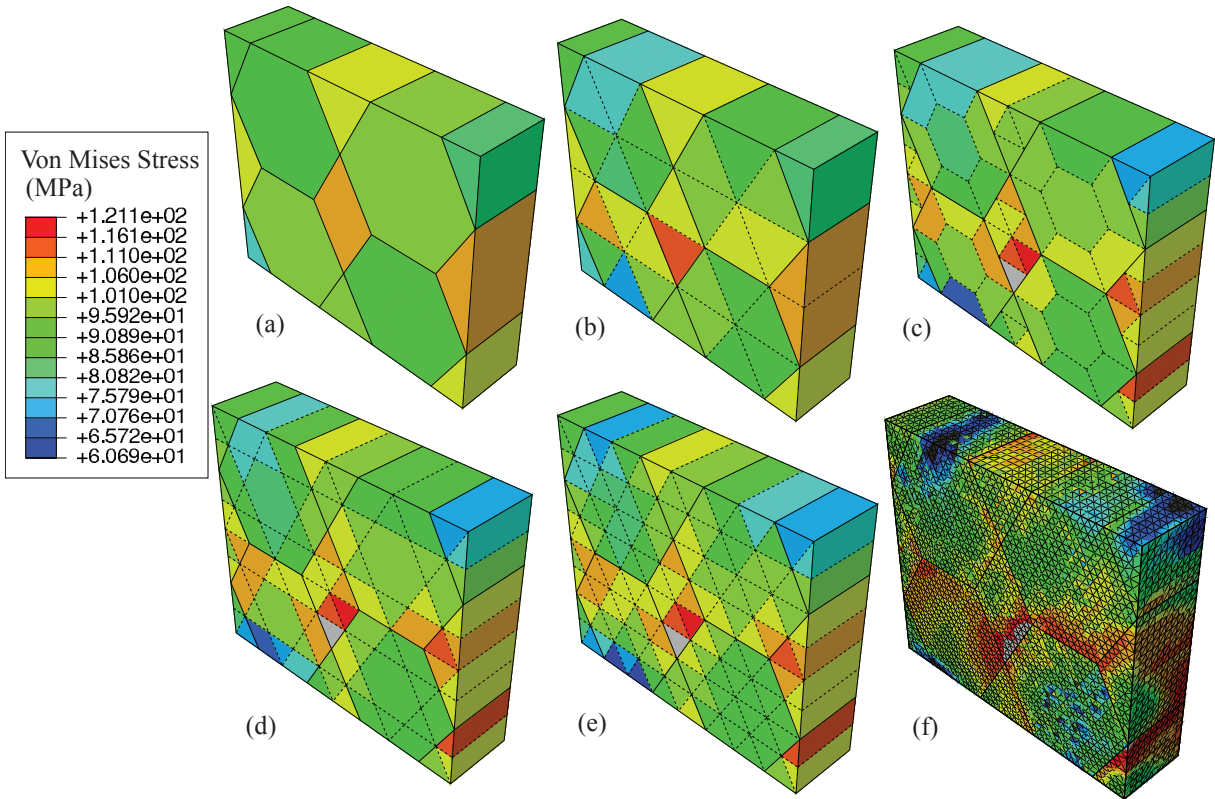


Figure 12: Local stress contours from: (a) DD-EHM grain partition; (b) DD-EHM triangular prism partition; (c) DD-EHM surface grain interaction pattern; (d) DD-EHM triple junction partition; (e) DD-EHM triangular partition with double precision; (f) CPFEM fully resolved mesh.

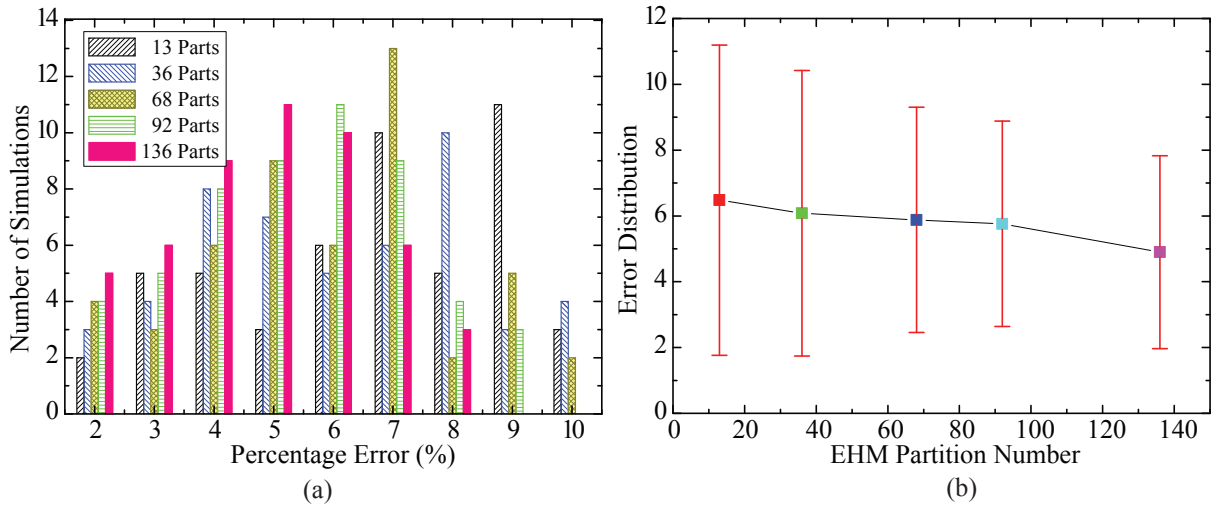


Figure 13: Statistical error analysis of overall stress prediction using all 50 sets of grain orientations: (a) error scattering pattern; (b) the stress error as a function of the DD-EHM model order.

363 is a function of the partition scheme, the sparsity of the matrix calculation and the grain
364 number, which were investigated in [22]. The computational speedup Q is 43 and 47 for BCC
365 and HCP cases, respectively, using the 145-grain RVE. The slight variation is due to differences
366 in number of iterations needed to convergence the equilibrium equations.

367 This study demonstrates that the hierarchical model improvement capability allows more
368 accurate model prediction with increasing model order, especially in better capturing the
369 local (e.g., sub-grain) fields. Assessment of this feature is important for characterization of
370 convergence of the reduced model to full CPFE simulations when sufficiently large number
371 of parts are used. However, the cost of simulations naturally increases with refinement of
372 the reduced order models. Efficiently employing hierarchical model improvement in structural
373 simulations also require adaptive model refinement algorithms, which will be investigated and
374 developed in the future.

375 4 DD-EHM simulation for near- α Ti-6242S

376 Ti-6242S, is a near- α titanium alloy that has been used in a variety of applications such as air-
377 craft structure and turbine engine compressor. This material exhibits high resistance to failure
378 associated with creep, fatigue and environmental degradation. Its hierarchical microstructure
379 exhibits characteristic features, such as the primary α grains, matrix of lamellar $\alpha+\beta$ and
380 microtextured regions of α particles with similar orientations, that contribute to the observed
381 mechanical and physical properties [60, 61, 62]. Alloying elements Al, Sn and Zr primarily
382 serve to stabilize the α phase, whereas Mo acts as a β phase stabilizer. Si is utilized to improve
383 the creep resistance at high temperature.

384 The experimental data of Ti-6242S in [59] is used as the input to generate the microstructure
385 and to calibrate the proposed EHM model. The chemical composition of the Ti-6242S material
386 is shown in Table 2. Here, the primary α occupies most of the material with the remainder
387 occupied by the β phase. The duplex annealing process is applied to obtain this microstructure.
388 The α phase has the crystal structure of HCP and the β phase is BCC. Above approximately
389 990 °C, the fully transformed beta phase could be obtained. Its melting temperature is about
390 1700 °C. Burgers orientation relationship (BOR) is usually observed in colony, Widmanstätten
391 or Basketweave structure inside the ($\alpha + \beta$) microstructure [63]. EBSD scans do not indicate
392 that equiaxed alpha/beta phase forms BOR inside this type of Ti-6242S.

393 Under service performance of cyclic loading, the inner dislocation behavior of plastic de-
394 formation in Ti-6242S is quite different from that during the forming process. Under ex-
395 perimental microscopy, a net dislocation accumulation is observed in each loading cycle of
396 high cycle fatigue and very high cycle fatigue loading, and generation and annihilation of
397 dislocations describes the nonlinear behavior and contributes to the onset of fatigue crack nu-
398 cleation [64]. In addition, low angle boundaries are observed in the titanium alloys during the
399 α to β phase transformation, which means that the sub-grain or dislocation substructure exists

400 inside individual grains [65]. In the micro-textured α/β colonies of titanium alloys, the sessile
401 dislocation storage or pile-ups is promoted by the crystallographic and morphological features
402 on both basal and prismatic slip, and mobile dislocation usually passes through the α/β in-
403 terface [66, 67]. Under cyclic loading conditions at room temperature, plastic deformations
404 are taken to be dominated by dislocation glide [68, 69]. Thus, the sub-grain sessile dislocation
405 storage inside individual crystal [35] and the reversal dislocation under cyclic loading [48] in-
406 troduced in Section 2.1 are applied here for better describing the dislocation mechanism inside
407 Ti-6242S. This alloy does not exhibit significant deformation twinning at the relatively small
408 strain levels [25].

409 4.1 DD-EHM calibration

410 The material used in this study follows ref. [59], which has 94 % stabilized primary α grains
411 with no micro-texture zones or α/β colonies. Thus, the influence of the β phase on the
412 mechanical response is relatively low [70]. In fact, the choice for the parameters for the beta
413 phase is relatively insensitive to stress-strain data employed in model calibration. Since the
414 volume fraction of β phase is low, the β -phase model is simplified by considering the same
415 parameters for all the BCC slip systems shown in Fig. 3. The model parameters for β grains
416 are chosen consistent with previous studies [71, 72].

417 The 3D polycrystalline RVEs are generated from 2D SEM images assuming identical fea-
418 tures in the orthogonal directions to the image. Experimentally characterized grain size dis-
419 tribution, grain orientation and misorientation distribution functions are employed in the con-
420 struction of the RVE to provide an accurate description of the crystallographic features. The
421 beta phase volume fraction is much lower than that of the alpha phase. Only 8 small grains
422 are identified as beta phase in the 145-grain RVE. Grain size distributions are fitted by two
423 continuous probability distribution functions, i.e., lognormal distribution $(\sigma, \mu) = (10.21, 0.16)$
424 for the β phase and normal distribution with cutoff $(\sigma, \mu) = (0.43, 1.74)$ for the α phase. The
425 chosen distribution functions are best fits to the experimental data provided in [59] as shown
426 in Figs. 14(c)-(d). Misorientation distribution and the pole figures from [59] are shown in
427 Fig. 14. The misorientation angle are the ones for each HCP grain boundaries. The misorien-
428 tation angles are divided into 36 bins with the bin size of 2.5 degrees. The volume fraction of
429 each bin is added up and collected into each bin. The misorientation distribution in the RVE
430 are enforced by using the misorientation probability assignment method (MPAM) introduced
431 by [71]. Consistent with the previous literatures [25, 73, 50], the evolution of sessile dislocation
432 densities in basal, prismatic and pyramidal slip systems of HCP and three types of BCC slip
433 systems are considered.

434 The cyclic response of the polycrystalline Ti-6242S is described using the aforementioned
435 dislocation density based crystal plasticity model. Two sets of information have been em-
436 ployed to calibrate the model parameters of crystal plasticity model. The first set consists of
437 the existing experimental datasets and corresponding calibrated models of Ti-6242S provided

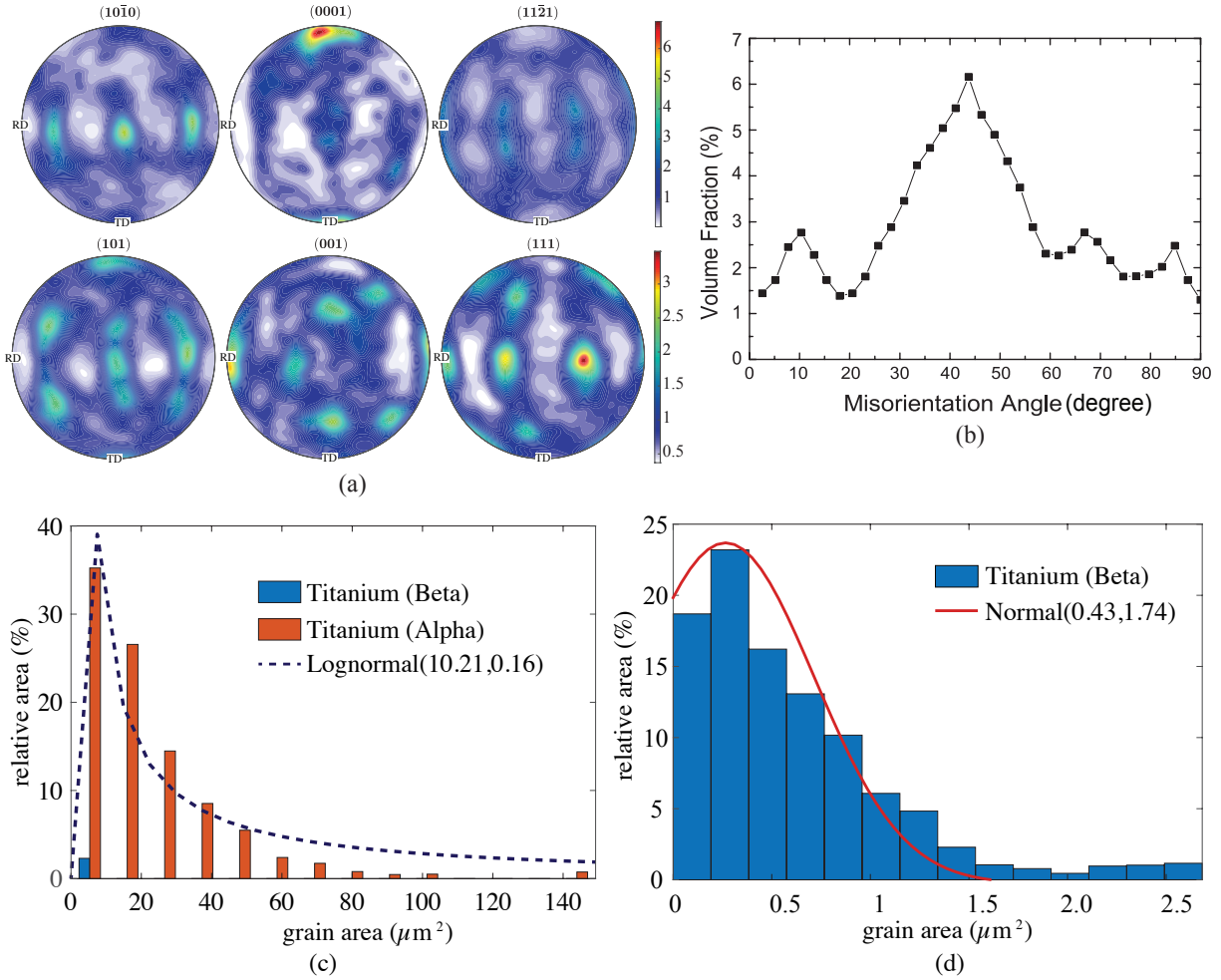


Figure 14: (a) Orientation distribution in pole figure; (b) Misorientation distribution for Ti-6242S data from [59]; (c) grain size distribution of α phase; and (d) grain size distribution of β phase.

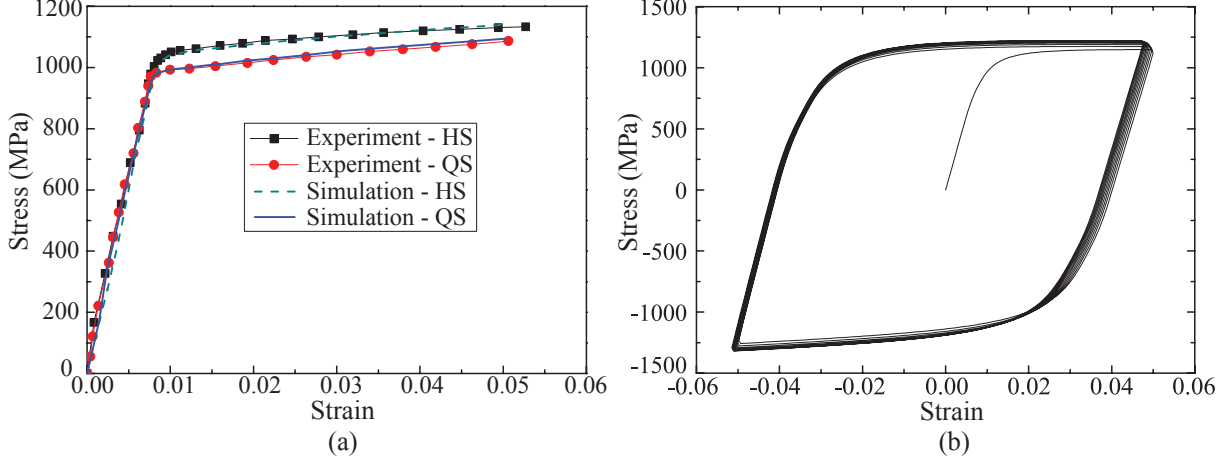


Figure 15: (a) Overall stress-strain behavior of Ti-6242S specimens from experiments and the calibrated DD-EHM model; (b) Stress-strain loops under cyclic loading.

438 in [71, 74, 25, 75, 72]. The experiments and model predictions of these studies have been
 439 fitted with the proposed dislocation density based model. The model parameters were then
 440 further tuned to accurately capture the stress-strain curves performed at two strain rates at
 441 room temperature [59]. A single set of material parameters are obtained by matching experi-
 442 mental datasets for quasi-static uniaxial tension experiments under two constant strain rates
 443 (QS: $8.33 \times 10^{-5} \text{ s}^{-1}$; HS: 0.01 s^{-1}) at room temperature, summarized in Table 3. Figure 15
 444 (a) shows the comparison of the stress-strain curves from the experiments and the calibrated
 445 model.

Table 2: Chemical composition in weight % of Ti-6242S [59].

Component	Al	Sn	Zr	Mo	Si	C	N	O
Measured	5.96	1.98	3.92	1.99	0.09	0.02	< 0.01	0.10

Table 3: Calibrated model parameters for Ti-6242S.

Parameters		Slip Systems				
Symbols	Units	Basal $\langle a \rangle$	Prismatic $\langle a \rangle$	Pyramidal $\langle a \rangle$	Pyramidal $\langle c + a \rangle$	BCC Slip
ΔF^s	J	3.95×10^{-20}	3.81×10^{-20}	4.27×10^{-20}	4.73×10^{-20}	3.74×10^{-20}
ΔV^s	m^3	5.91×10^{-29}	8.20×10^{-29}	7.40×10^{-29}	8.85×10^{-29}	6.30×10^{-29}
k	$\text{J} \cdot \text{K}^{-1}$	1.381×10^{-23}	1.381×10^{-23}	1.381×10^{-23}	1.381×10^{-23}	1.381×10^{-23}
ρ_m	m^{-2}	5.00×10^{12}	5.00×10^{12}	5.00×10^{12}	5.00×10^{12}	5.00×10^{12}
ν_{id}	Hz	1.00×10^{12}	1.00×10^{12}	1.00×10^{12}	1.00×10^{12}	1.00×10^{12}
b^s	μm	2.94×10^{-4}	2.95×10^{-4}	2.95×10^{-4}	4.68×10^{-4}	2.86×10^{-4}
k_1^s	m^{-1}	1.80×10^7	1.68×10^7	1.67×10^7	2.40×10^7	1.03×10^7
D^s	MPa	300	330	100	90	230

446 RVE size convergence is investigated using both CPFEM and DD-EHM models to identify
 447 the proper size of the RVE that adequately resolves the local response fields under cyclic

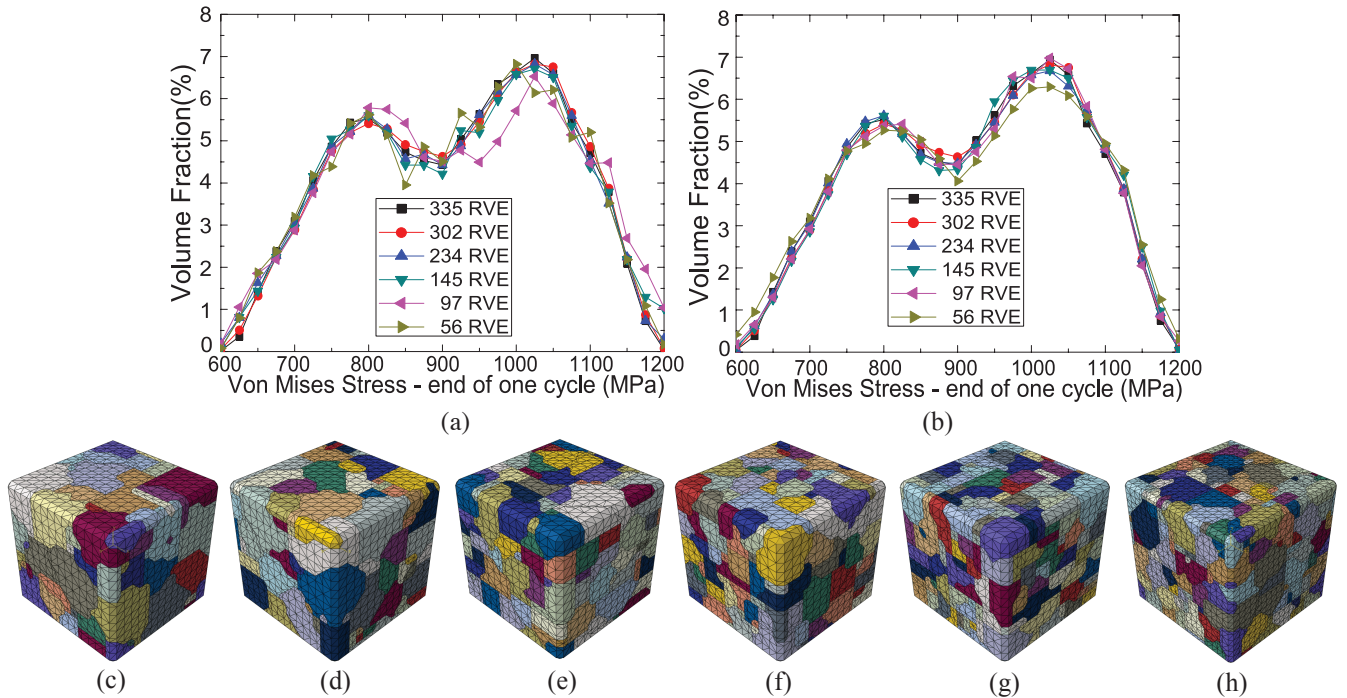


Figure 16: Local stress distribution as a function of RVE size: (a) DD-EHM model; (b) CPFEM model for RVEs with (c) 56 grains; (d) 97 grains; (e) 145 grains; (f) 245 grains; (g) 302 grains; and (h) 335 grains.

448 loading. Figure 16 shows the distribution of local stresses within the RVE as a function of RVE
 449 size (ranging from 56 to 335 grains). Figure 15 (b) shows that the stress-strain loops stabilize
 450 quickly under a pure fatigue load cycle by approximately the eighth cycle. The variation of
 451 the response fields is slight from cycle to cycle. Figure 16(a,b) captures the stress distributions
 452 at the peak of the first load cycle. Using both models, the local response of the microstructure
 453 converges when the edge length of RVE is larger than $19.58 \mu\text{m}$ (i.e., 145 grains). Thus, the
 454 145-grain microstructure is deemed representative for the overall mechanical response. Since
 455 CPFEM resolves the microstructure response, the stress distribution is smoother than that of
 456 the DD-EHM.

457 4.2 Structural-scale simulation of near- α titanium during cyclic 458 loading

459 The capabilities of the proposed reduced order modeling approach in capturing crystal-scale
 460 characteristics is further assessed using structural simulation. The structural domain is an L-
 461 shaped bracket made of Ti-6242S. The geometry, discretization and the boundary conditions
 462 used for the structural scale problem are shown in Fig. 17. Displacement-controlled cyclic
 463 loading is applied at the anchors of the bottom edge. The applied displacement rate and
 464 maximum displacement amplitude are 12 mm/s and 3 mm, respectively. The geometry is
 465 discretized used 3,940 tri-linear eight-node hexahedral elements. Reduced order integration is

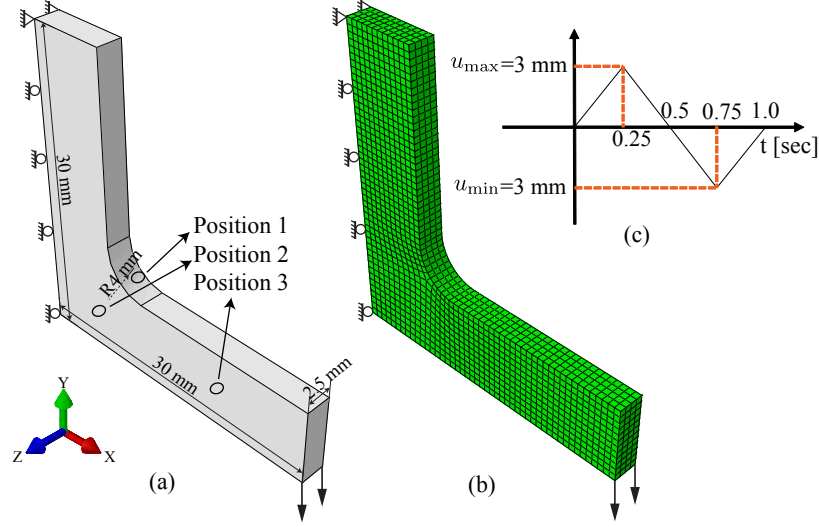


Figure 17: A L-shape plate of Ti-6242S under strain controlled cyclic loading: (a) geometry and loading condition of the plate; (b) finite element mesh; (c) strain-controlled loading history.

466 employed with hourglass control to alleviate zero energy modes. Each quadrature point of the
 467 macroscale mesh is associated with a microstructure that consists of 145 grains with the edge
 468 length of $19.58 \mu\text{m}$ as shown in Fig. 16e. Identical microstructures have been used at each
 469 quadrature point. The simulation therefore tracks the response of a total of 571,300 grains.
 470 Simulations have been performed using the *one-part-per-grain* model reduction strategy. The
 471 simulation of the structure using the classical computational homogenization approach or the
 472 direct resolution (i.e., CPFEM) of the microstructure is computationally prohibitive, therefore
 473 not included in this study.

4.2.1 Dislocation pile-ups at two spatial scales

474
 475 Transmission electron microscopy of Ti-6242S specimen indicate intense dislocation pile-ups
 476 at the grain boundaries slightly beneath the crack nucleation surface [68, 69]. Using scanning
 477 electron microscopy on the same material, the dislocation pile-ups are revealed as the zigzag
 478 boundary between hard and soft grain pairs [76]. Prior numerical investigations using CPFEM
 479 identified that the dislocation pile-up length is a critical parameter indicating fatigue crack
 480 nucleation [75, 20]. Accumulated dislocation pile-ups could induce crack nucleation through
 481 multiple mechanisms, including slip band localization [77, 78], stress concentrations at the
 482 alpha/alpha grain boundaries or at the alpha/beta phase boundaries [79] and basal stress
 483 concentration in the neighboring hard grain due to load shedding phenomenon inside hard-
 484 soft grain pairs [80, 81, 82].

485 The experimental observations of Ti-6242S show that the dislocations prefer to directly
 486 transfer through the alpha/beta phase boundary [68]. Strong slip bands do not occur during the
 487 low-cycle fatigue loading [69] Thus, we assume that the dislocation pile-ups at the alpha/alpha
 488 grain boundary has the main effect on crack nucleation. The amount of pile-ups is quantified

489 by the relative dislocation density discrepancy $\Delta\rho_{\text{tot}}$ between neighboring grain pairs (Fig. 18).
 490 Since the plastic anisotropy of HCP crystal is involved and the slip system activation is mainly
 491 dominant by a single type of slip system [83, 43, 31], hence, the maximum dislocation pile-ups
 492 is obtained in the slip system with the highest sessile dislocation density regardless of the slip
 493 system type and the order of slip system.

494 The maximum relative dislocation density discrepancy in an RVE is obtained using the
 495 following steps:

- 496 1. At the beginning of the simulation: For each grain in the microstructure, identify all the
 497 neighboring grains that share surface facets with the grain to form the grain pairs.
- 498 2. During the simulation at a given load increment:
 - 499 (a) For each grain, i , within the RVE, the maximum dislocation density is obtained by
 500 looping over all the slip systems ($s = 1, \dots, n$) inside the grain.

$$(\rho_{\text{tot}})^i = \max_{s \in \{1, \dots, N\}} \{(\rho_{\text{tot}}^s)^i\} \quad (21)$$

- 501 (b) For each grain, i , maximum dislocation discrepancy is set to the largest difference
 502 between the maximum dislocation density in grain i and that of all its neighboring
 503 grains ($j = 1, \dots, m_i$), where m_i is the total number of neighbors of grain i .

$$(\Delta\rho_{\text{tot}})^i = \max_{j \in \{1, \dots, m_i\}} \left\{ \left| (\rho_{\text{tot}})^i - (\rho_{\text{tot}})^{k(j)} \right| \right\} \quad (22)$$

504 where, $k(j)$ is the grain ID for the j^{th} neighbor of grain i .

- 505 (c) Maximum dislocation discrepancy in the entire RVE is chosen as the highest value
 506 of the maximum dislocation discrepancies of all grains i within the RVE:

$$\Delta\rho_{\text{tot}} = \max_{i \in \{1, \dots, n\}} \{(\Delta\rho_{\text{tot}})^i\} \quad (23)$$

507 The time evolution of relative dislocation density distributions are reported from three
 508 different spatial positions within the structure as illustrated in Fig. 17a. Figure 19 shows
 509 the microstructure-maximum relative dislocation density distributions at six time instances
 510 at the three spatial positions (the time instances are identified in the inset figure). Two
 511 key observations are that the relative dislocation densities exhibit significant spatiotemporal
 512 variations and that the peak relative dislocation densities do not necessarily coincide with
 513 the peak loads (i.e., $t = 0.25$ s and $t = 0.75$ s). The spatial variations shown in Fig. 18a
 514 are naturally due to geometrically induced non-uniform stresses within the structure, but the
 515 spatial distributions also significantly change as a function of applied displacement amplitude
 516 and time due to load redistributions induced by viscoplasticity. At peak applied displacement
 517 amplitude (at $t = 0.25$ s), very small amount of plastic deformation and dislocation generation
 518 are observed at positions 2 and 3, whereas many of the grains undergo plastic deformation and

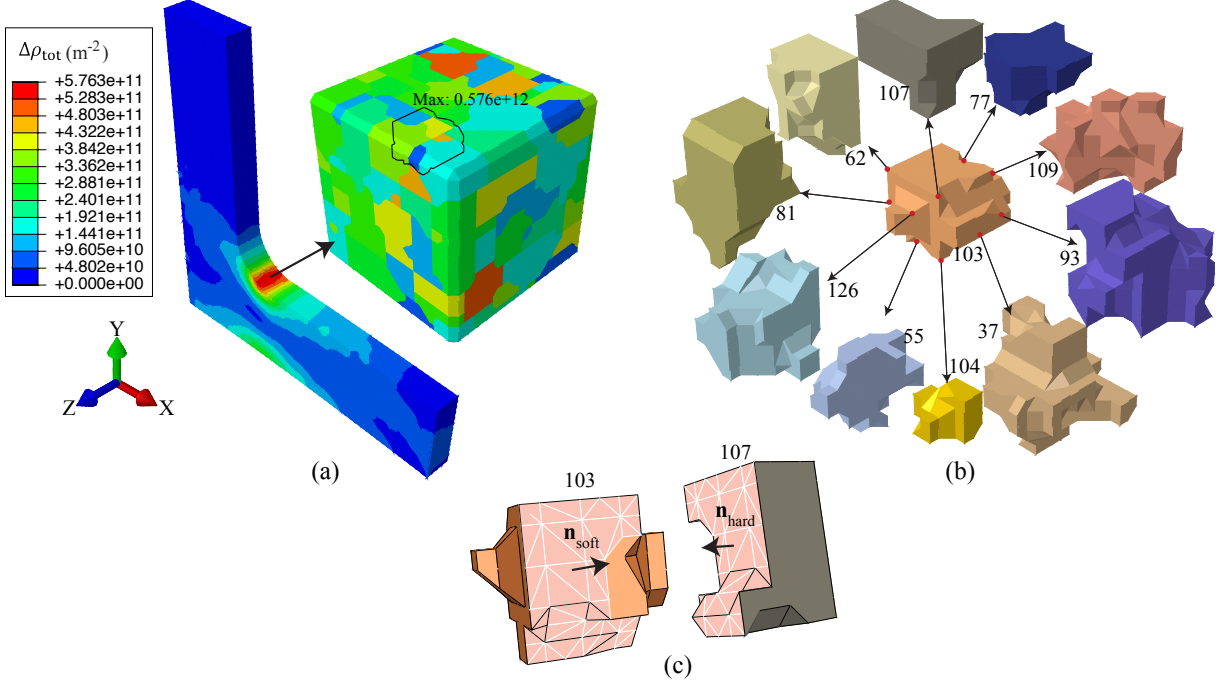


Figure 18: Schematic illustration of capturing dislocation pile-ups at grain boundary: (a) extract $\Delta\rho_{tot}$ of a microstructure at a given macroscopic integration point; (b) identify neighboring grains according to adjacent nodes; (c) potential crack interface.

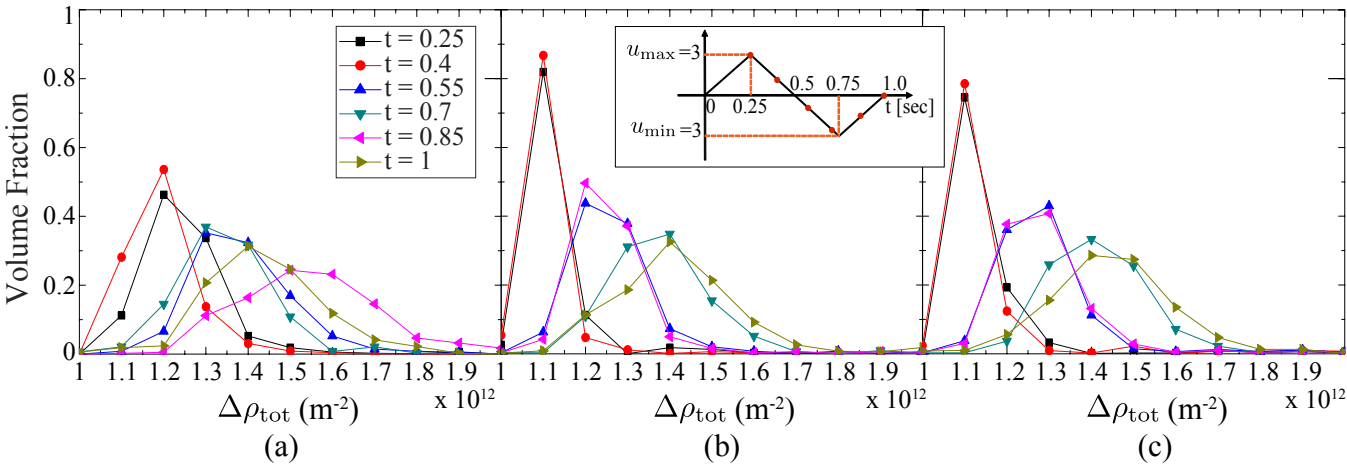


Figure 19: $\Delta\rho_{tot}$ distribution at different time steps in: (a) position 1; (b) position 2; (c) position 3. The insert shows the loading profile and the red dots in the black curves represent the displacement history at $t = 0.25, 0.4, 0.55, 0.7, 0.85, 1.0$ sec.

519 dislocation generation at position 1. The unloading and reloading (in the opposite direction)
520 processes demonstrate a non-monotonic growth of relative dislocation density indicating a non-
521 monotonic increase in dislocation pile-up. At the end of the loading process, (at $t = 1.0$ s),
522 a much wider range of relative dislocation density levels are observed in position 1 compared
523 with the positions 2 and 3. It is important to note that the tail ends of the distributions are
524 likely to be more indicative of failure nucleation process than the distribution means, since
525 failure is likely to nucleate near a few grains with high degree of dislocation pile-up.

526 4.2.2 Effect of non-uniform texture

527 Strain partitioning due to non-uniform texture is widely observed in the experimental studies
528 of titanium alloys [84, 85, 86]. The strong anisotropic HCP crystals enhance strain localization
529 due to hard or soft crystallographic orientations [87]. Recent studies suggested small clusters
530 of similar crystal orientations, called micro-textured regions (MTR) or macrozones, can have
531 a significant effect on the fatigue and dwell fatigue sensitivities in titanium alloys, even though
532 no severe texture is observed in the experiments [88, 89]. However, the non-uniform texture
533 could have the potential benefit of reducing the strain localization in specific locations, which
534 might be a critical region during the service of the structural component. Through a selection
535 of non-uniform texture, it might be possible to alleviate or defer crack nucleation in critical
536 spots of the components.

537 In this section, three different texture orientations are selected and assigned to different
538 parts of the L-shape component in Fig. 20a to form a non-uniform textured structure. In part
539 1, the α grain orientation selection in the RVE remains the same as the experiments by [59],
540 and the dominant direction of crystal c-axis is along the Y axis. The orientations in part 2 and
541 3 are such that the dominant c-axis directions are along Z and X axes, respectively. Same
542 strain-controlled load is applied as shown in Fig. 17b. The L-shape geometry and the loading
543 location at the edge result in a inhomogeneous stress distribution within the component.
544 However, Fig. 20b shows compression- or tension-like behaviors (along X axis) at the top and
545 bottom of the adjacent area between part 1 and part 2. The high stress levels at these spots
546 contribute to local plastic slip and the corresponding strain concentration shown in Fig. 21a
547 and b. Due to the geometry of the fillet, higher stress localization is observed and leads to more
548 severe plastic deformation at the top area. While the texture of the component considered
549 in this example is artificial, this study allows us to investigate the effect of microtexture, and
550 demonstrate the capability of DD-EHM in quantifying the effect of microtextured regions at
551 the scale of a structural component.

552 The high spot zone of strain distribution occurs in part 1 and it diminishes in part 2
553 in Fig. 21(b), whereas high strains are observed in both part 1 and part 2 in the original
554 case. This is due to different dominant crystallographic orientations. Part 1 and 2 form a
555 stress-state at the macro-scale similar to that near the hard-soft grain boundary observed at
556 micro-scale. The crystal c-axis of part 1 is mainly perpendicular to the direction of maximum

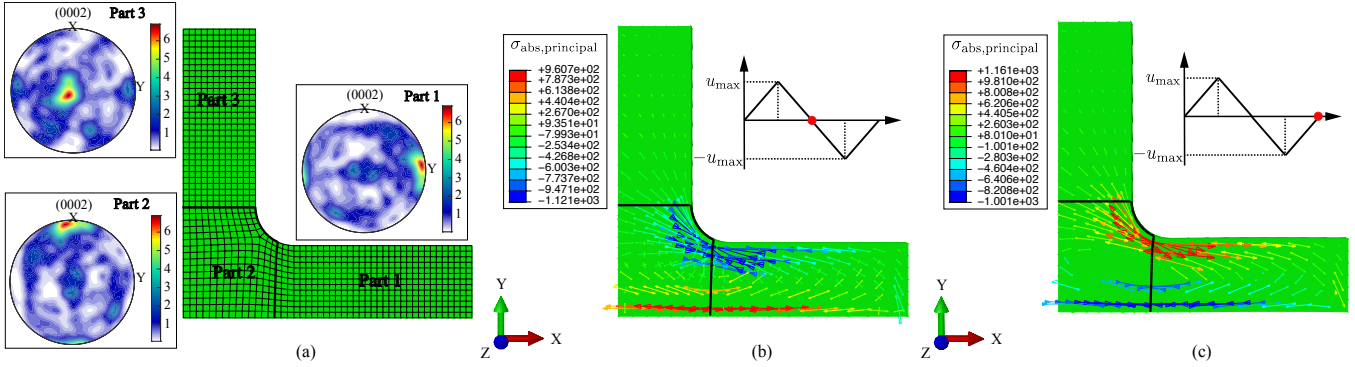


Figure 20: (a) Non-uniform texture selections in three separate parts of L-shape component; (b) the directions of maximum principal stress at the middle of the cycle; (c) the directions of maximum principal stress at the end of the cycle. $\sigma_{\text{abs,principal}}$ refers to the maximum principal value compared using absolute value.

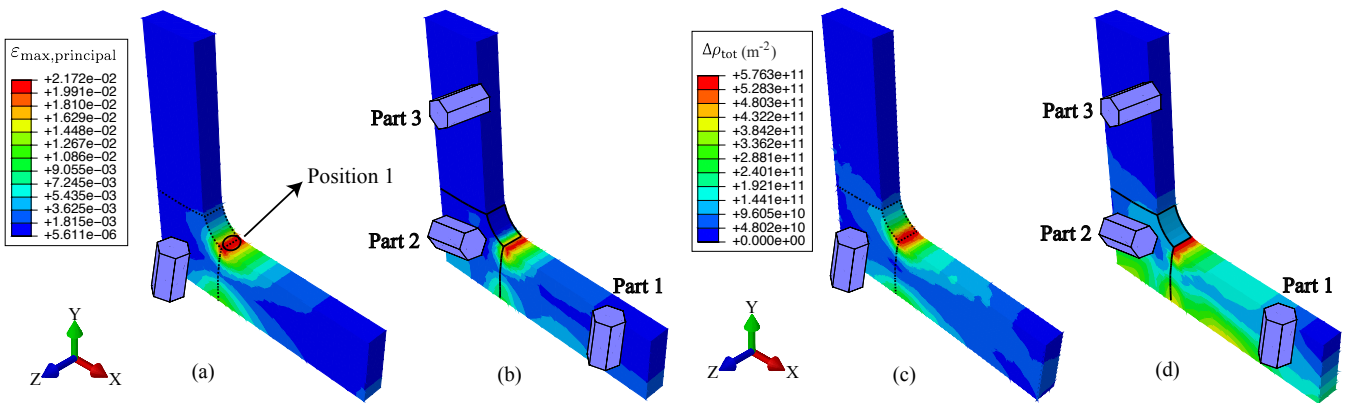


Figure 21: Maximum principal strain $\epsilon_{\text{max,principal}}$ and $\Delta\rho_{\text{tot}}$ distributions in L-shape panel: uniform-texture case from experiments (a and c); non-uniform-texture case (b and d). The hexagonal prism indicate the dominant grain orientation

557 principal stress which favors the prismatic dislocation activation to trigger the plastic slip
558 near boundary of part 1 and 2, but only localized at part 1. In contrast, the c -axis of part 2
559 is nearly parallel to the local load. Prismatic and basal dislocations are hard to activate at
560 this crystal configuration and it needs much higher stresses to overcome the energy barrier of
561 pyramidal slip. Thus, much less plastic deformation is observed in part 2 compared with part
562 1. This strain partitioning phenomenon is analogous to the observations in the micro-textured
563 regions of titanium [84, 62]. Individual hard or soft grains in the microstructure could not
564 form the macro-scale strain partitioning. As the plastic slip is blocked in part 2, it could not
565 be transferred to part 3 and no plastic deformation is observed in part 3.

566 The maximum dislocation pile-ups inside hard-soft grain pairs are also investigated for the
567 non-uniform-texture case in Fig. 21d. It is observed that the high dislocation pile-up is only
568 observed in part 1. The bottom area of the panel contributes more dislocation pile-ups in the
569 macro-scale hard-soft texture pairs than that in the uniform-texture case, which is consistent
570 with the strain distribution. The reduction in strain and dislocation pile-up in part 2 indicate
571 that non-uniform texture selections could be used to alleviate the local strain concentration
572 and crack nucleation.

573 5 Conclusions

574 This manuscript presented an extension of the EHM approach to gain the ability to perform
575 multiscale simulations of titanium alloy structures coupling the scale of representative volumes
576 that resolve polycrystalline microstructure to the structural scale. The proposed approach was
577 verified for accuracy in modeling the behavior of HCP and BCC polycrystals. This manuscript
578 also investigated the evolution of dislocation pile-ups at grain boundaries, which serves as an
579 important factor for fatigue crack nucleation in titanium alloys. The following main conclusions
580 are drawn from our investigations:

- 581 • The DD-EHM approach is extended to the HCP and BCC based polycrystal plasticity.
582 A reversible dislocation density based model is utilized to capture physics beneath the
583 crystal anisotropy and plastic slip during cyclic loading. RVE-level investigations on
584 HCP and BCC polycrystal verify the macro- and micro-scale accuracy of the method.
- 585 • The DD-EHM approach demonstrates high accuracy when compared with the CPFEM
586 approach, but with significantly lower computational cost, allowing for relatively large
587 structural scale simulations and accounting for grain interactions. The accuracy in cap-
588 turing the localized behavior at sub-grain-scale is improved by proper selection of the
589 reduced basis through appropriate microstructure partitioning.
- 590 • Structural simulations on an L-shape panel shows that texture orientation has an impor-
591 tant influence on the strain distribution, and could be leveraged at the structural scale
592 to reduce strain concentrations and dislocation pile-ups thereby improving fatigue life.

593 The reduced order modeling approach, as well as the multi-scale fatigue nucleation modeling
594 will be advanced in a number of fronts in the near future. Firstly, this manuscript focused
595 on the verification of the EHM approach in the context of material behavior that does not
596 exhibit severe strain softening. The presence of strain softening results in the formation of
597 localization bands with length scales that may be lower than the size of the RVE. The EHM
598 methodology will be extended to address problems that exhibit this phenomenon. Next, the
599 proposed dislocation pile-up parameter is not the only factor in fatigue crack nucleation. It
600 is reasonable to demonstrate a criterion of the combination of the dislocation pile-up and
601 basal stress to predict the I-type crack nucleation observed in titanium under fatigue or dwell
602 fatigue loading condition. The multi-scale fatigue nucleation site prediction approach will also
603 be extended for life predictions and validated against experimental observations.

604 **6 Acknowledgments**

605 Part of the research has been performed with research funding from Air Force Office of Scientific
606 Research (Grant No: FA9550-13-1-0140. Program Manager: Jamie Tiley), which is gratefully
607 acknowledged. The authors thank Dr. Brian T. Gockel for sharing the experimental data
608 originally published in [59]. The authors also acknowledge the discussions with Dr. Adam
609 Pilchak that contributed to the analyses presented in this manuscript. The lead author has
610 conducted this research at Vanderbilt University through the financial support of the China
611 Scholarship Council (No. 201606060105), which is gratefully acknowledged.

612 **References**

- 613 [1] Feyel F and Chaboche J L 2000 *Comput. Meth. Appl. Mech. Engrg.* **183** 309–330
- 614 [2] Oskay C and Fish J 2007 *Comput. Meth. Appl. Mech. Engrg.* **196** 1216–1243
- 615 [3] Oskay C 2012 *Int. J. Numer. Meth. Engng.* **89** 686–705
- 616 [4] Oskay C 2013 *Comput. Meth. Appl. Mech. Engrg.* **264** 178–190
- 617 [5] Zhang S and Oskay C 2015 *Comput. Mech.* **55** 771–787
- 618 [6] Weinan E, Engquist W B E and Huang Z 2003 *Phys. Rev. B* **67** 92–101
- 619 [7] Masud A and Scovazzi G 2011 *Int. J. Numer. Meth. Fluids* **65** 28–42
- 620 [8] Efendiev Y and Hou T Y 2009 *Multiscale Finite Element Methods* (Springer)
- 621 [9] Mosby M and Matous K 2016 *Extreme. Mech. Lett.* **6** 68–74
- 622 [10] Shanthraj P, Eisenlohr P, Diehl M and Roters F 2015 *Int. J. Plast.* **66** 31 – 45

- 623 [11] Van Houtte P, Li S, Seefeldt M and Delannay L 2005 *Int. J. Plast.* **21** 589–624
- 624 [12] Knezevic M, McCabe R J, Lebensohn R A, Tomé C N, Liu C, Lovato M L and Mihaila
625 B 2013 *J. Mech. Phys. Solids.* **61** 2034–2046
- 626 [13] Pandey A, Kabirian F, Hwang J H, Choi S H and Khan A S 2015 *Int. J. Plast.* **68** 111–131
- 627 [14] Zecevic M and Knezevic M 2015 *Int. J. Plast.* **72** 200–217
- 628 [15] Lebensohn R, Kanjarla A and Eisenlohr P 2012 *Int. J. Plast.* **32–33** 59–69
- 629 [16] Michel J and Suquet P 2004 *Comput. Meth. Appl. Mech. Engrg.* **193** 5477–5502
- 630 [17] Michel J and Suquet P 2016 *J. Mech. Phys. Solids.* **90** 254–285
- 631 [18] Zhang H, Diehl M, Roters F and Raabe D 2016 *Int. J. Plast.* **80** 111 – 138
- 632 [19] Anahid M and Ghosh S 2013 *Int. J. Plast.* **48** 111–124
- 633 [20] Ozturk D, Kotha S, Pilchak A L and Ghosh S 2019 *J. Mech. Phys. Solids.* **128** 181–207
- 634 [21] Zhang X and Oskay C 2015 *Comput. Meth. Appl. Mech. Engrg.* **297** 408–436
- 635 [22] Zhang X and Oskay C 2017 *Comput. Meth. Appl. Mech. Engrg.* **326** 241–269
- 636 [23] Zhang S and Oskay C 2016 *Comput. Meth. Appl. Mech. Engrg.* **300** 199–224
- 637 [24] Zhang S and Oskay C 2017 *Comp. Mech.* **59** 887–907
- 638 [25] Ghosh S and Anahid M 2013 *Int. J. Plast.* **47** 182 – 201
- 639 [26] Zhang Z and Dunne F P 2018 *Int. J. Fatigue* **113** 324 – 334 ISSN 0142-1123
- 640 [27] Michel J and Suquet P 2003 *Int. J. Solids Struct.* **40** 6937–6955
- 641 [28] Cottrell A H 1954 *Dislocations and Plastic Flow in Crystals* (American Association for
642 the Advancement of Science)
- 643 [29] Friedel J 1964 *Dislocations* (Pergamon Oxford)
- 644 [30] Hirth J P and Lothe J 1968 *Theory of Dislocations* (New York: McGraw-Hill)
- 645 [31] Beyerlein I and Tomé C 2008 *Int. J. Plast.* **24** 867–895
- 646 [32] Madec R, Devincere B and Kubin L 2002 *Phys. Rev. Lett.* **89** 255508
- 647 [33] Viguier B, Hemker K J, Bonneville J, Louchet F and Martin J L 1995 *Philos. Mag A* **71**
648 1295–1312

- 649 [34] Ardeljan M, Beyerlein I J and Knezevic M 2014 *J. Mech. Phys. Solids.* **66** 16–31
- 650 [35] Liu Y, Zhu Y, Oskay C, Hu P, Ying L and Wang D 2018 *Mater. Sci. Eng. A* **724** 298–323
- 651 [36] Le K and Tran T 2017 *Phys. Rev. E* **96** 013004
- 652 [37] Le K, Tran T and Langer J 2018 *Scr. Mater.* **149** 62–65
- 653 [38] Le K and Tran T 2018 *Phys. Rev. E* **97** 043002
- 654 [39] Hu P, Liu Y, Zhu Y and Ying L 2016 *Int. J. Plast.* **86** 1 – 25
- 655 [40] Zheng Z, Waheed S, Balint D S and Dunne F P 2018 *Int. J. Plast.* **104** 23–38
- 656 [41] Ghosh S, Shahba A, Tu X, Huskins E L and Schuster B E 2016 *Int. J. Plast.* **87** 69 – 85
- 657 [42] Knezevic M, Lebensohn R A, Cazacu O, Revil-Baudard B, Proust G, Vogel S C and Nixon
658 M E 2013 *Mater. Sci. Eng. A* **564** 116–126
- 659 [43] Ardeljan M, Knezevic M, Nizolek T, Beyerlein I J, Mara N A and Pollock T M 2015 *Int.*
660 *J. Plast.* **74** 35–57
- 661 [44] Oppedal A L, El Kadiri H, Tomé C N, Kaschner G C, Vogel S C, Baird J C and Horste-
662 meyer M F 2012 *Int. J. Plast.* **30-31** 41–61
- 663 [45] Naka S, Lasalmonie A, Costa P and Kubin L P 1988 *Philos. Mag A* **57** 717–740
- 664 [46] Fan X and Yang H 2011 *Int. J. Plast.* **27** 1833 – 1852
- 665 [47] F Louchet L P K and Vesely D 1979 *Philos. Mag. A* **39** 433–454
- 666 [48] Kitayama K, Tomé C, Rauch E, Gracio J and Barlat F 2013 *Int. J. Plast.* **46** 54–69
- 667 [49] Follansbee P S and Gray G T 1989 *Metall. Trans. A* **20** 863–874
- 668 [50] Zhang Z, Jun T S, Britton T B and Dunne F P 2016 *J. Mech. Phys. Solids.* **95** 393 – 410
- 669 [51] Mecking H and Kocks U 1981 *Acta Mater.* **29** 1865 – 1875
- 670 [52] Appel F, Lorenz U, Oehring M, Sparka U and Wagner R 1997 *Mater. Sci. Eng. A* **233** 1
671 – 14
- 672 [53] Williams W S and Schaal R D 1962 *J. Appl. Phys.* **33** 955–962
- 673 [54] Zhang X and Oskay C 2016 *Modelling Simul. Mater. Sci. Eng.* **24** 055009
- 674 [55] Phan V, Zhang X, Li Y and Oskay C 2017 *Mech. Mater.* **114** 215–227

- 675 [56] Benzing J, Liu Y, Zhang X, Luecke W, Ponge D, Dutta A, Oskay C, Raabe D and Wittig
676 J 2019 *Acta Mater.* **177** 250 – 265
- 677 [57] Barbe F, Quey R, Musienko A and Cailletaud G 2009 *Mech. Res. Commun.* **36** 762–768
- 678 [58] Kelley E and Hosford W 1968 *Trans. Met. Soc. AIME* **242** 5–13
- 679 [59] Gockel B T, Kolesar R S and Rollett A D 2016 *Integr. Mater. Manuf. Innov.* **5** 13
- 680 [60] Pilchak A L, Li J and Rokhlin S I 2014 *Metall. Mater. Trans. A* **45** 4679–4697
- 681 [61] Pilchak A L, Shank J, Tucker J C, Srivatsa S, Fagin P N and Semiatin S L 2016 *Integr.*
682 *Mater. Manuf. Innov.* **5** 14
- 683 [62] Ma R, Pilchak A L, Semiatin S L and Truster T J 2018 *Int. J. Plast.* **107** 189–206 ISSN
684 07496419
- 685 [63] Dunne F P E and Rugg D 2008 *Fatigue Fract. Eng. Mater. Struct.* **31** 949–958
- 686 [64] Castelluccio G M, Musinski W D and McDowell D L 2016 *Int. J. Fatigue* **93** 387 – 396
- 687 [65] Huang L, Chen Y, Kong F, Xu L and Xiao S 2013 *Mater. Sci. Eng. A* **577** 1 – 8
- 688 [66] Suri S, Viswanathan G, Neeraj T, Hou D H and Mills M 1999 *Acta Mater.* **47** 1019 –
689 1034
- 690 [67] Savage M F, Tatalovich J and Mills M J 2004 *Philos. Mag* **84** 1127–1154
- 691 [68] Joseph S, Bantounas I, Lindley T C and Dye D 2018 *Int. J. Plast.* **100** 90 – 103
- 692 [69] Joseph S, Lindley T C and Dye D 2018 *Int. J. Plast.* **110** 38–56 ISSN 07496419
- 693 [70] Satko D P, Shaffer J B, Tiley J S, Semiatin S L, Pilchak A L, Kalidindi S R, Kosaka Y,
694 Glavicic M G and Salem A A 2016 *Acta Mater.* **107** 377 – 389
- 695 [71] Deka D, Joseph D S, Ghosh S and Mills M J 2006 *Metall. Mater. Trans. A* **37** 1371–1388
- 696 [72] Venkatramani G, Ghosh S and Mills M 2007 *Acta Mater.* **55** 3971–3986
- 697 [73] Dunne F, Walker A and Rugg D 2007 *Proc. Royal Soc. A* **463** 1467–1489
- 698 [74] Ghosh S, Anahid M and Chakraborty P 2011 *Modeling Fatigue Crack Nucleation Us-*
699 *ing Crystal Plasticity Finite Element Simulations and Multi-time Scaling* (Boston, MA:
700 Springer)
- 701 [75] Ozturk D, Shahba A and Ghosh S 2016 *Fatigue Fract. Eng. Mater. Struct.* **39** 752–769

- 702 [76] Sinha V, Jha S K, Pilchak A L, Porter W J, John R and Larsen J M 2017 *Metall. Mater.*
703 *Trans. A* **6** 261–269
- 704 [77] Lin M, Fine M and Mura T 1986 *Acta Metall.* **34** 691–628
- 705 [78] Ahmed J, Wilkinson A and Roberts S 2001 *Philos. Mag. A* **81** 1473–1488
- 706 [79] Tanaka K and Mura T 1981 *J. Appl. Mech.* **48** 97–103
- 707 [80] Stroh A 1954 *Proc. R. Soc. Lond. A* **223** 404–414
- 708 [81] Evans W and Bache M 1994 *Int. J. Fatigue* **16** 443–452
- 709 [82] Benjamin B T and Wilkinson A J 2012 *Acta Mater.* **60** 5773–5782 ISSN 13596454
- 710 [83] Kirane K and Ghosh S 2008 *Int. J. Fatigue* **30** 2127 – 2139
- 711 [84] Echlin M P, Stinville J C, Miller V M, Lenthe W C and Pollock T M 2016 *Acta Mater.*
712 **114** 164–175
- 713 [85] Huang M, Xu C, Fan G, Maawad E, Gan W, Geng L, Lin F, Tang G, Wu H, Du Y, Li
714 D, Miao K, Zhang T, Yang X, Xia Y, Cao G, Kang H, Wang T, Xiao T and Xie H 2018
715 *Acta Mater.* **153** 235–249
- 716 [86] Gorji M B, Tancogne-Dejean T and Mohr D 2018 *Acta Mater.* **148** 442–455
- 717 [87] Britton T B, Dunne F P E and Wilkinson A J 2015 *Proc. R. Soc. Lond. A* **471** 164–175
- 718 [88] Lunt D, Xu X, Busolo T, Fonseca J Q and Preuss M 2018 *Scr. Mater.* **145** 45–49
- 719 [89] Lunt D, Busolo T, Xu X, Fonseca J Q and Preuss M 2017 *Scr. Mater.* **129** 72–82